Delft University of Technology

Neural-adaptive constrained flight control for air ground recovery under terrain obstacles

Su, Zikang; Wang, Xinwei; Wang, Honglun

Citation (APA)

Important note
To cite this publication, please use the final published version (if applicable).
Please check the document version above.

Neural-adaptive constrained flight control for air-ground recovery under terrain obstacles

Zikang Su, Xinwei Wang and Honglun Wang

Abstract—**This paper contrives a neural-adaptive constrained controller of the cable towed air-ground recovery system subject to terrain obstacles, unmeasurable cable tensions, trailing vortex, wind gust, and actuator saturation. In air-ground recovery system modeling, the towed vehicle's nominal 6 DOF affine nonlinear dynamics and the cable system's finite links-joints dynamics are formulated. To achieve accurate air-ground recovery under terrain obstacles, an asymmetric barrier Lyapunov function-based flight controller of the towed vehicle is proposed, by transforming the terrain obstacles into time-varying constraints on the vehicle's trajectory. Then, to approximate the towed vehicle's lumped unknown dynamics caused by the unmeasurable cable tensions and airflows, several echo state network (ESN) approximators are established for velocity and attitude subsystems. By using the state approximation errors-based neural weights learning strategy and minimal learning parameter technique (MLP), these ESNs possess better transient behaviors and lower online computational burden. sss Furthermore, the actuator saturation is automatically monitored and released, by incorporating a specially designed auxiliary compensating system into the angular rate control law for compensation. The stability of the closed-loop system is analyzed. Finally, numerical simulations under two air-ground recovery scenarios are performed to demonstrate the performance of the proposed controller.**

Index Terms—**air-ground recovery, towed vehicle, constrained flight control, neural approximation, actuator saturation.**

I. INTRODUCTION

The air recovery of valuable payloads or targets without landing will considerably enhance the operational effectiveness and flexibility in remote dangerous regions [1]. The air-ground recovery system has been proposed for the payload pickup mission in remote dangerous regions. This

technique employs a cable towed vehicle with active aerodynamic surfaces to hook an immobile ground target [2]. This kind of aerial towed cable system has many applications, such as air pickup system [3], probe-drogue aerial refueling system [4,5], aerial recovery system [6], sonar arrays [7], towed target [8,9], and terrain-following [10]. The towed air-ground recovery system not only can access remote areas that cannot be reached by helicopters but also can avoid the recovery danger caused by the landing of the rapid thrust aircraft [11]. The system consists of a towing aircraft, a flexible cable, and a towed vehicle. During the air-ground recovery, the payloads or targets on the ground will be retrieved with the towed cable-vehicle system. The cable towed vehicle (skyhook) with active aerodynamic control surfaces is accurately controlled to promptly pick up the ground target. Consequently, the accurate trajectory control of the flexibly towed vehicle, subjecting to multiple mission/physical constraints, unmeasurable cable tensions, airflows, and actuator saturation, plays a key role in a successful air-ground recovery.

To address the air-ground recovery problem, some practical and theoretical attempts have been made. A famous air-ground recovery application, known as Fulton skyhook, was developed to recover crew from remote locations [12]. The Fulton Skyhook uses a "skyanchor" on the aircraft's nose to hook onto a rope hoisted by a helium balloon attached to the ground target. The aircraft is required to fly close to the ground and to provide the picks-up guidance. The later researches use an aerial towed cable-vehicle system to recover the ground target [2]. These approaches generally can be concluded as two different categories: passive and active strategies. The passive strategy indirectly guides the towed vehicle without control surfaces to rendezvous with the ground target, by extra path plan and control of the towing aircraft [1,2,11]. Williams *et al.* [11] and Nichols *et al.* [13] recovery the ground target and air target by a circularly towed cable system to achieve an approximatively stationary trajectory of the cable tip, respectively. Williams *et al.* [2] also researched the air-ground recovery under terrain obstacles and wind gust, by the optimal path planning of a cable towed in a level flight. But the control accuracy of the passive vehicle cannot be guaranteed due to the flexible cable's dynamics. In contrast, the active strategy uses control surfaces to directly guide the vehicle's trajectory, which avoids the extra complexity of the active strategy. The active vehicle adopts control surfaces to directly provide necessary aerodynamic forces and moments to efficiently regulate its trajectory. The active strategy applications can be found in aerial recovery [6],

towed flight vehicles [8,9], terrain-following [10], and aerial refueling drogue [14]. In the air-ground recovery, little research on the towed vehicle's active control can be found. To our knowledge, Jun *et al.* [3] proposed a linear quadratic digital regulator (LQR) method to guide the active vehicle to accurately pick up a stationary ground target. But this approach has not concurrently considered the problem of the terrain obstacles, airflows, actuator saturation, and the control coupling between the cable and vehicle.

The particularity of the air-ground recovery mission decides some unavoidable issues [2,3]: 1) the terrain obstacles avoidance should be considered to adapt more complex practically air-ground recovery environments; 2) the unmeasurable towing cable tensions and the unavoidable airflows (including aircraft's trailing vortex, wind gust, etc.) will induce extra undesirable unknown dynamics of the cable and towed vehicle; 3) the aerodynamic actuator saturation of the towed vehicle may occur in the presence of the maneuvering, towing and airflows. To take all of these issues into consideration, the trajectory controller of the towed vehicle should simultaneously possess high accuracy trajectory constrained control ability, robust performance against unknown dynamics, and reliable saturation releasing mechanism.

To achieve accurate air-ground recovery under terrain obstacles, Williams *et al.* [2] assumed the air-ground recovery cable system was towed by a level flying aircraft. Then, they used multiple-phase pseudospectral methods to plan the optimal trajectory of the aircraft under terrain obstacles and variable gusts. However, this path planning-based approach is one passive strategy, which is difficult for online implementation because of the applied SNOPT solver with a great computational burden [2]. Moreover, the trajectory control accuracy of the cable tip cannot be exactly guaranteed via the indirect guidance of the flexibly towed cable. Inspired by the recently developed nonlinear constrained control theory [15,16], we innovatively solve terrain obstacle avoidance problems during the air-ground recovery with a constrained flight trajectory control method. This method transforms the terrain obstacle violations into time-varying trajectory constraints of the towed vehicle. The asymmetric barrier Lyapunov function (aBLF) based backstepping, proposed by Tee *et al.* [17], provides an alternative approach to handle the asymmetric time-varying output constraints. The time-varying aBLF is used to guarantee the accurate tracking of the outputs (or the states) to command signals without violating the predefined constraints space. Moreover, the dynamic surface control (DSC) [6,18-20] is used to address the "explosion of complexity" inherit from backstepping design.

To enhance the performance robustness of the flight control system, many methodologies have been proposed, such as disturbance-observer-based control (DOBC) [21,22], composite hierarchical anti-disturbance control (CHADC) [23], adaptive techniques [24], and neural networks (NN) [25,26]. The basic idea of the DOBC framework [21,22], which has been applied to many flight control systems, is to estimate the external disturbance with disturbance observer and then compensate in the feed-forward channel. Chen proposed a nonlinear disturbance-observer (NDO) based dynamic inversion approach for the missile to enhance the performance robustness against uncertain aerodynamic coefficients [27]. Yang *et al.* [28] employed the nonlinear DOBC to handle the robust flight control problem for the longitudinal dynamics of airbreathing hypersonic vehicles (AHV) under mismatched disturbances. This approach can achieve satisfactory robustness against mismatched disturbances and model uncertainties of AHV. Wang *et al.* [29] used the nonlinear disturbance observer to effectively estimate and compensate for the unknown disturbances in the attitude coordination control problem for spacecraft. Similar to the DOBC framework, Zhou *et al.* [30] presented a fixed-time observer to estimated fault/disturbance for safety control of quadrotor. Under the DOBC framework, to further improve the control precision against multiple disturbances, Guo [23,31] firstly proposed the CHADC. The CHADC consists of two parts: disturbance observer for estimation and the baseline controller for a nominal system. It has also been applied to many flight control scenarios, such as the AHV [32] and quadrotor [33,34]. To handle the towed drogue stabilization problem in aerial recovery, Su *et al.* [6] proposed high order sliding mode observer-based DSC trajectory controller to stabilize the cable towed drogue.

For the flight control of the towed drogue in air-ground recovery, the unknown nonlinear dynamics caused by the towing tension and turbulent airflows occupy the majority proportion of the entire dynamics of the towed vehicle. Moreover, these considerable unknown dynamics are not only coupling with the nominal dynamics in the same channel but also coupling with the dynamics in different channels of the velocity loop and attitude loop. Considering the NN has been proved to be a powerful tool to online approximate the unknown dynamics of nonlinear systems [25,26,35], it provides another effective solution to enhance the performance robustness of the towed vehicle in air-ground recovery subject to the unmeasurable cable tensions and airflows. Among the neural networks, a kind of named echo state network (ESN) has shown its superior capability for nonlinear dynamics approximation [36-40]. It possesses two unique parts of weights: a hidden layer (dynamical reservoir) with sparsely and randomly interconnected neurons and a memoryless output layer (readout). The ESN provides an easier approach to supervised training of recurrent NN with ease training and precision approximation without changing weights between the input layers and the hidden layers [37,38]. However, with the increasing number of parameters to be tuned online within the adaptive ESN approximators (i.e., the neural weights of the hidden layer), its computationally learning burden will considerably increase [26,41,42]. Unfortunately, limited hardware computational capability may result in certain time delays during the learning process, which may not be tolerable for maneuvering flight in air-ground recovery under terrain obstacles. How to release the time-consuming online learning process of ESN for the vehicle's unknown dynamics approximation should be considered. Inspired by the minimal learning parameter (MLP) technique which uses the maximum

norm of neural weight to replace its components vectors in classical NN [41,42], we incorporate MLP into ESN to markedly reduce the online computational burden for the approximation. Then, the MLP based ESN (MLPESN) approximator can be constructed to approximated and compensate the towed vehicle's unknown dynamics caused by the unmeasurable cable tensions and airflows, without much online computational burden.

For the control actuator saturation problem in the towing flight control, auxiliary systems have been presented to deal with the input constraints by compensating for the desired control laws [42-46]. However, the parameter tuning of the auxiliary system is complex. Thus, Bu *et al.* [47] proposed a new auxiliary system with only two parameters for flight control, and this system can provide a proper choice for actuator saturation induced by the winds or cable tensions in air-ground recovery.

Inspired by the above observations, we proposed a neural-adaptive constrained flight controller for the towed air-ground recovery system subject to terrain obstacles, unmeasurable cable tensions, airflows, and actuator saturation. The main contributions are summarized as follows:

(1) A neural-adaptive constrained flight controller is proposed for the air-ground recovery system subject to terrain obstacles, unmeasurable cable tensions, trailing vortex, wind gust, and actuator saturation.

(2) An aBLF based trajectory constrained control strategy is innovatively presented for the terrain obstacles avoidance during air-ground recovery, by transforming the terrain obstacle violations into time-varying constraints on the towed vehicle's trajectory. Furthermore, the actuator saturation is automatically addressed in angular rate control law with the aid of a specially designed auxiliary system.

(3) By learning the neural weights with state estimation errors, the MLPESN approximator, which not only improves the transient approximation behaviors but also decreases the online computational burden without offline training, is established to approximate to accurately approximate the lumped unknown dynamics caused by unmeasurable cable tensions and airflows.

The layout of the paper is as follows. Sec. II formulates the air-ground recovery problem under terrain obstacles. Sec. III comprehensively illustrates the proposed MLPESN approximator-based constrained flight controller for the air-ground recovery. Sec. IV conducts numerical simulation verifications under two scenarios. Sec. V concludes the paper.

II. PROBLEM FORMULATION

A. Lumped Mass Dynamics of the Towed Cable System

The air-ground recovery system is assumed to be towed by a level flying aircraft with constant altitude H_0 and velocity V_0. The towed vehicle is equipped with active aerodynamic control surfaces.
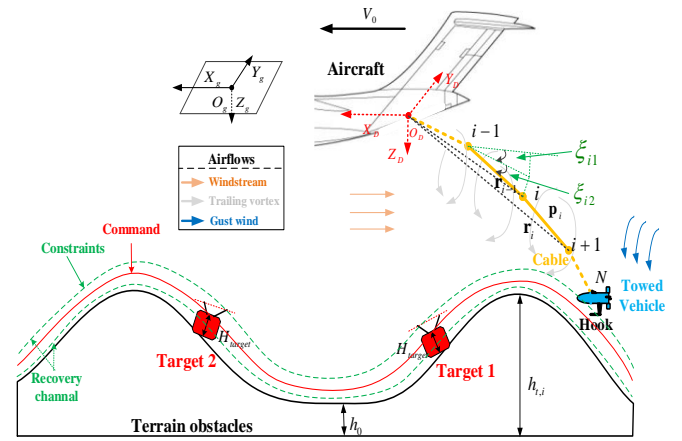

Fig. 1. The diagram of the cable-vehicle air-ground recovery system.

The towed cable system's lumped mass dynamics can be formulated with finite rigid joints and variable-length links [2,6,8], as shown in Fig. 1. The frictionless cable joint concentrates the mass and loads of the connecting link, where $i = 1, ..., N$ is the index of the joints, and N is the total link number. The towing axis $O_D - X_D Y_D Z_D$ is aligned with the inertial frame axis $O_g - X_g Y_g Z_g$. In the towing axis, $\mathbf{p}_i$ denotes the position vector of link i, $\mathbf{r}_i$ denotes the position vector of joint i from the origin O_D, ξ_{i1} and ξ_{i2} are the vertical and lateral deflection angle of link $i-1$, respectively.

Referring to the dynamics of the towed cable system [2,6,8], the dynamics of $\xi_{ij}, (i = 1, 2, ..., N, j = 1, 2)$ can be formulated as

$$\ddot{\xi}_{ij} = \frac{\mathbf{p}_{i,\xi_{ij}}}{\left(\mathbf{p}_{i,\xi_{ij}} \cdot \mathbf{p}_{i,\xi_{ij}}\right)} \begin{bmatrix} \mathbf{a}_i - \mathbf{a}_{i-1} - \mathbf{p}_{i,l_i} \ddot{l}_i - \dot{\mathbf{p}}_{i,l_i} \dot{l}_i - \\ \sum_{j=1}^{2} \left(\dot{\mathbf{p}}_{i,\xi_{ij}} \dot{\xi}_{ij}\right) - \boldsymbol{\alpha}_i \times \mathbf{p}_i - \boldsymbol{\omega}_i \times \dot{\mathbf{p}}_i \end{bmatrix}, \quad (1)$$

$$i = 1, ..., N, j = 1, 2$$

where $\mathbf{p}_i = -l_i \mathbf{n}_i = -l_i \left[c_{\xi_{i1}} c_{\xi_{i2}}, s_{\xi_{i2}}, -s_{\xi_{i1}} c_{\xi_{i2}} \right]$, $l_i = \left(L_0 / N\right)$, L_0 is the total cable length, $\mathbf{n}_i$ is the direction of link i, $s_{(\cdot)} = \sin(\cdot), c_{(\cdot)} = \cos(\cdot)$; $\mathbf{p}_{i,\xi_{ij}} = \partial \mathbf{p}_i / \partial \xi_{ij}, \mathbf{p}_{i,l_i} = \partial \mathbf{p}_i / \partial l_i$; $\mathbf{a}_i = \mathbf{a}_{i-1} + \ddot{\mathbf{p}}_i$ is the acceleration of joint i ; $\boldsymbol{\omega}_i, \boldsymbol{\alpha}_i$ are the rotational angular velocity and angular acceleration of $O_D - X_D Y_D Z_D$ to $O_g - X_g Y_g Z_g$.

To solve the dynamics Eq. (1), the following cable tension constraint equations should be included [6], [8].

$$\left(\mathbf{n}_i \cdot \mathbf{n}_{i-1}\right) T_{i-1} / m_{i-1} - \left(1 / m_{i-1} + 1 / m_i\right) T_i + \left(\mathbf{n}_i \cdot \mathbf{n}_{i+1}\right) T_{i+1} / m_i$$
$$= \ddot{l}_i - l_i \dot{\mathbf{n}}_i \cdot \mathbf{n}_i - \left(\left(\mathbf{G}_{i-1} + \mathbf{Q}_{i-1}\right) / m_{i-1} - \left(\mathbf{G}_i + \mathbf{Q}_i\right) / m_i\right) \mathbf{n}_i \quad (2)$$

where m_i is the mass of joint i ; $T_i = \|\mathbf{T}_i\|$, $\mathbf{G}_i$ and $\mathbf{Q}_i$ are the tension, gravity, and aerodynamic force on joint i, and

$$\mathbf{Q}_i = \left(\mathbf{D}_i + \mathbf{D}_{i-1}\right)/2, i = 1,...,N-1$$

$$\mathbf{Q}_N = 0.5\mathbf{D}_N + 0.5\rho\mathbf{V}_{aN}/\|\mathbf{V}_{aN}\|^3 S_V c_d^0 \qquad (3)$$

$$\mathbf{D}_i = \begin{pmatrix} \left(-0.5\rho\left(\mathbf{V}_{ai}\cdot\mathbf{n}_i\right)^2 \pi d_c l_i c_T\right)\mathbf{n}_i - \\ \left(0.5\rho\left(\mathbf{V}_{ai}-\left(\mathbf{V}_{ai}\cdot\mathbf{n}_i\right)\mathbf{n}_i\right)d_c l_i c_n\right)\times \\ \left(\mathbf{V}_{ai}-\left(\mathbf{V}_{ai}\cdot\mathbf{n}_i\right)\mathbf{n}_i\right) \end{pmatrix}$$

where ρ is the air density; $\mathbf{V}_{ai}$ is the wind vector around link i; c_d^0 and S_V are the towed vehicle's basic drag coefficient and reference area; d_c, c_T and c_n are the cable's diameter, skin friction coefficient, and drag coefficient.

B. Towed Vehicle's Affine Nonlinear Dynamics and Disturbances Analysis

The acceleration of joint N can be described as follows

$$\mathbf{a}_N = \left(\mathbf{G}_N + \mathbf{G}_V + \mathbf{Q}_N + \mathbf{T}_N + \mathbf{F}_a\right)/m_{NV} \qquad (4)$$

where $m_{NV} = m_N + m_V$ is the total mass of cable tip (including joint N and vehicle), $\mathbf{G}_V$ is the gravity of the towed vehicle.

Define the following state vectors for towed vehicle

$$\mathbf{X}_1 = \frac{1}{V_0}\begin{bmatrix} y \\ z \end{bmatrix}, \mathbf{X}_2 = \frac{1}{V_0}\begin{bmatrix} V_y \\ V_z \end{bmatrix}, \mathbf{X}_3 = \begin{bmatrix} \phi \\ \beta \\ \alpha \end{bmatrix}, \mathbf{X}_4 = \begin{bmatrix} p \\ q \\ r \end{bmatrix},$$

$$\mathbf{U}_{act} = \begin{bmatrix} \delta_a \\ \delta_e \\ \delta_r \end{bmatrix}, \mathbf{X}_1^A = \begin{bmatrix} x \\ y \\ z \end{bmatrix}, \mathbf{X}_2^A = \begin{bmatrix} V_x \\ V_y \\ V_z \end{bmatrix}, \mathbf{X}_3^P = \begin{bmatrix} \beta \\ \alpha \end{bmatrix} \qquad (5)$$

where V_0 is the normalized velocity, x, y, z and V_x, V_y, V_z are trajectories and velocities in $O_g - X_g Y_g Z_g$; β, α, ϕ are the angle of sideslip, angle of attack and roll angle; p, q, r are the roll, pitch, and yaw angular rates; $\delta_a, \delta_e, \delta_r$ are the deflections of the aileron, elevator, and rudder.

Considering the tension $\mathbf{T}_N$ provides driven forces for the unpowered vehicle towed by cable, its nominal 6 DOF affine nonlinear dynamics can be established [6,9,49] as follows.

$$\dot{\mathbf{X}}_1^A = \frac{1}{V_0}\begin{bmatrix} \dot{x} \\ \dot{y} \\ \dot{z} \end{bmatrix} = \frac{1}{V_0}\begin{bmatrix} 1 & 0 & 0 \\ 0 & 1 & 0 \\ 0 & 0 & 1 \end{bmatrix}\begin{bmatrix} V_x \\ V_y \\ V_z \end{bmatrix} = \mathbf{X}_2^A \qquad (6)$$

$$\dot{\mathbf{X}}_2^A = \frac{1}{V_0}\begin{bmatrix} \dot{V}_x \\ \dot{V}_y \\ \dot{V}_z \end{bmatrix} = \underbrace{\frac{1}{m_{NV}V_0}\begin{bmatrix} T_{Nx}^I + Q_{Nx}^I \\ T_{Ny}^I + Q_{Ny}^I \\ T_{N2}^I + Q_{Nz}^I \end{bmatrix}}_{\mathbf{F}_2^A} - \underbrace{\frac{\bar{Q}S_V}{m_{NV}V_0}\begin{bmatrix} 0 & 0 & 0 \\ 0 & c_Y^\beta & 0 \\ 0 & 0 & -c_L^\alpha \end{bmatrix}\begin{bmatrix} \phi \\ \alpha \\ \beta \end{bmatrix}}_{\mathbf{H}_2^A}$$

$$+ \underbrace{\frac{\bar{Q}S_V}{m_{NV}V_0}\begin{bmatrix} 0 & 0 & 0 \\ 0 & c_Y^\beta & 0 \\ 0 & 0 & -c_L^\alpha \end{bmatrix}\begin{bmatrix} \phi \\ \beta \\ \alpha \end{bmatrix}}_{\mathbf{B}_2^A} = \begin{bmatrix} F_{Vx} \\ F_{Vy} \\ F_{Vz} \end{bmatrix} + \begin{bmatrix} H_{Vx} \\ H_{Vy} \\ H_{Vz} \end{bmatrix} + \mathbf{B}_2^A\mathbf{X}_3 \qquad (7)$$

$$= \mathbf{F}_2^A + \mathbf{H}_2^A + \mathbf{B}_2^A\mathbf{X}_3$$

$$\dot{\mathbf{X}}_3 = \begin{bmatrix} \dot{\phi} \\ \dot{\beta} \\ \dot{\alpha} \end{bmatrix} = \left\{ \underbrace{-\begin{bmatrix} 0 & \frac{s_\phi s_\beta}{c_\beta} & \frac{c_\phi s_\beta}{c_\beta} \\ s_\alpha & 0 & -c_\alpha+1 \\ -\frac{s_\beta c_\alpha}{c_\beta} & 0 & -\frac{s_\beta s_\alpha}{c_\beta} \end{bmatrix}\begin{bmatrix} p \\ q \\ r \end{bmatrix}}_{\mathbf{H}_3} + \underbrace{\begin{bmatrix} 1 & 0 & 0 \\ 0 & 0 & -1 \\ 0 & 1 & 0 \end{bmatrix}\begin{bmatrix} p \\ q \\ r \end{bmatrix}}_{\mathbf{B}_3} + \underbrace{\begin{bmatrix} 0 \\ \frac{G_y^W + T_{Ny}^W + Y}{m_{NV}V_{aN}} \\ \frac{G_z^W + T_{Nz}^W - L}{m_{NV}V_{aN}c_\beta} \end{bmatrix}}_{\mathbf{F}_3} \right\} \qquad (8)$$

$$= \begin{bmatrix} F_\phi \\ F_\beta \\ F_\alpha \end{bmatrix} + \begin{bmatrix} H_\phi \\ H_\beta \\ H_\alpha \end{bmatrix} + \mathbf{B}_3\mathbf{X}_4 = \mathbf{F}_3 + \mathbf{H}_3 + \mathbf{B}_3\mathbf{X}_4$$

$$\dot{\mathbf{X}}_4 = \begin{bmatrix} \dot{p} \\ \dot{q} \\ \dot{r} \end{bmatrix} = \underbrace{\begin{bmatrix} \frac{I_z\bar{Q}S_V bc_{\mathcal{L}}^0 + \left(I_y I_z - I_z^2\right)rq}{I_x I_z} \\ \frac{\bar{Q}S_V \bar{c}c_{\mathcal{M}}^0 + \left(I_z - I_x\right)pr}{I_y} \\ \frac{I_x\bar{Q}S_V bc_{\mathcal{N}}^0 + \left(I_x^2 - I_x I_y\right)pq}{I_x I_z} \end{bmatrix}}_{\mathbf{H}_4}$$

$$+ \underbrace{\bar{Q}_0 S_V \begin{bmatrix} bc_{\mathcal{L}}^{\delta_a}/I_x & 0 & 0 \\ 0 & \bar{c}c_{\mathcal{M}}^{\delta_e}/I_y & 0 \\ 0 & 0 & bc_{\mathcal{N}}^{\delta_r}/I_z \end{bmatrix}}_{\mathbf{B}_4}\mathbf{U}_{act} \qquad (9)$$

$$= \mathbf{H}_4 + \mathbf{B}_4\mathbf{U}_{act}$$

where $\left[T_{Nx}^I, T_{Ny}^I, T_{Nz}^I\right]$ and $\left[Q_{Nx}^I, Q_{Ny}^I, Q_{Nz}^I\right]$ are cable tensions and aerodynamic forces in the inertial frame; G_y^W, G_z^W and T_{Ny}^W, T_{Nz}^W are the corresponding gravity and cable tension components in winding frame; $\bar{Q} = 0.5\rho V_{aN}^2$, V_{aN} denotes the airspeed of the vehicle; Y, L are the lateral and lift aerodynamic forces; b and $\bar{c}$ are the vehicle's wingspan and mean aerodynamic chord; $\mathbf{F}_2 = \begin{bmatrix} F_{Vy}, F_{Vz} \end{bmatrix}^T$, $\mathbf{H}_2 = \begin{bmatrix} H_{Vy}, H_{Vz} \end{bmatrix}^T$, $\mathbf{B}_2 = \begin{bmatrix} c_Y^\beta, 0; 0, -c_L^\alpha \end{bmatrix}\bar{Q}S_V/m_{NV}$.

From the above formulation (2), the tensions $\left[T_{Nx}^I, T_{Ny}^I, T_{Nz}^I\right]$ and aerodynamic forces $\left[Q_{Nx}^I, Q_{Ny}^I, Q_{Nz}^I\right]$ are unknown nonlinear dynamics in the velocity subsystem (7), because of the unmeasurable characteristic of the cable towing tensions and turbulent airflows (including wind gust, trailing vortex, etc.). Thus, $\mathbf{F}_2^A$ acts as the major unknown dynamics in the velocity subsystem, $\mathbf{H}_2^A$ can be regarded as the nominal

dynamics in the velocity subsystem. Similarly, in attitude loop (8), $\mathbf{F}_3 = \left[0, \left(G_y^W + T_{Ny}^W + Y \right), \left(G_z^W + T_{Nz}^W - L \right) / c_\beta \right]^T / \left(m_{NV} V_{aN} \right)$ acts as the major unknown dynamics, and $\mathbf{H}_3$ can be regarded as the nominal dynamics. For the angler rate dynamics (9), there no explicit expressions related to the unmeasurable towing tensions and turbulent airflows. Thus, it can be assumed that no unknown dynamics in the angle rate subsystem, and $\mathbf{H}_4$ can be taken as the nominal dynamics.

Remark 1. It can be observed from dynamics (6)-(9) that the unknown nonlinear dynamics $\mathbf{F}_j$, $j = 2,3$ caused by the towing tension and airflows occupy the majority proportion. Moreover, these considerable unknown dynamics are coupling with the dynamics in different channels in the velocity loop and attitude subsystem. This is also the main reason and motivation for selecting the MLPESN approximator, which possesses powerful online approximation ability of the unknown dynamics [36-40], to approximate the unknown dynamics in the velocity and attitude subsystem.

C. Terrain Obstacles and Time-varying Trajectory Constraints Transformation

This work considers the air-ground scenarios with terrain obstacles, where the cable towed vehicle must be controlled to hook the ground target without hitting the terrain obstacles.

For simplicity, the terrain in the vertical direction is formulated as the sinusoidal function of the vehicle's forward trajectory x in line with [2]. $k = 1, ..., K_{to}$

$$z_{terrain} = \begin{cases} -h_{t,k} \sin\left(\pi \dfrac{x - x_{to,2k-1}}{x_{to,2k} - x_{to,2k-1}} \right), & x_{to,2k-1} \leq x \leq x_{to,2k} \\ -h_0, & \text{otherwise} \end{cases} \quad (10)$$

where $z_{terrain}$ is the vertical terrain obstacles in the inertial axis; $k = 1, ..., K_{to}$ is the sequence number of terrain obstacles, $h_{t,k}$ is the height of terrain obstacle k, h_0 is the level altitude except obstacles, $x_{to,2k}$ and $x_{to,2k+1}$ are the start and end forward coordinates of terrain obstacle k.

To ensure the exact hook without hitting the terrain obstacles, the command trajectory signals y_c, z_c for the towed vehicle can be established with the height of the target payloads H_{target} and Eq. (10).

$$\begin{cases} y_c(x) = 0 \\ z_c(x) = z_{terrain} - H_{target} \end{cases} \quad (11)$$

For the safety and success of the air-ground recovery, the time-varying vertical trajectory constraints can be predefined as Eq. (12), based on the command z_c and the safe height tolerances $\bar{H}_{tolerant}, \underline{H}_{tolerant}$.

$$\begin{cases} \bar{z}_c(x) = z_c(x) - \bar{H}_{tolerant} \\ \underline{z}_c(x) = z_c(x) + \underline{H}_{tolerant} \end{cases} \quad (12)$$

where $\bar{z}_c$ and $\underline{z}_c$ are the upper and lower constraints on the vehicle's vertical trajectory.

Moreover, the initial lateral deviation between the vehicle and command y_c probably exists, and this should be eliminated smoothly and quickly for accurate recovery hooking. To regulate the initial lateral trajectory deviation with prescribed convergence performance, the time-varying lateral trajectory constraints are designed as Eq. (13).

$$\begin{cases} \bar{y}_c(x) = (y_0 - y_\infty) e^{(-\ell x / V_0)} + y_\infty \\ \underline{y}_c(x) = -\bar{y}_c(x) \end{cases} \quad (13)$$

where y_0 is the predefined maximum overshoot of the lateral tracking error $e_y = y - y_c$; $\bar{y}_c(x)$ is bounded and strictly monotonically decreasing to the state boundary y_∞ which also determines the maximum steady-state error; and ℓ determines the convergence speed of $\bar{y}_c(x)$.

Besides, the actuator saturations (aileron δ_a, elevator δ_e, and rudder δ_r), which are described as Eq. (14), may occur in the presence of the maneuvering, cable's towing, and airflows.

$$\delta_j = \begin{cases} \bar{\delta}_j, & \delta_{jc} \geq \bar{\delta}_j \\ \delta_{jc}, & \underline{\delta}_j \leq \delta_{jc} \leq \bar{\delta}_j, \quad j = a,e,r \\ \underline{\delta}_j, & \delta_{jc} \leq \underline{\delta}_j \end{cases} \quad (14)$$

where $\bar{\delta}_j, \underline{\delta}_j, j = a,e,r$ are the maximum and minimum values of the corresponding actuator deflections; $\delta_{jc}, j = a,e,r$ are the corresponding actuator commands from the designed control law.

Therefore, the task can be concluded as establishing a neural-adaptive constrained flight controller for the towed vehicle subjects to terrain constraints (12)-(13), actuator saturation (14), unmeasurable cable tension, and airflows.

III. MLPESN APPROXIMATOR BASED CONSTRAINED FLIGHT CONTROL FOR TOWED VEHICLE

In this section, we give the detailed design process of the MLPESN approximator-based constrained flight controller for the towed vehicle subject to terrain obstacles, unmeasurable cable tensions, trailing vortex, wind gust, and actuator saturation. As shown in Fig.2, the proposed MLPESN approximator based constrained flight controller consists of two sections: 1) the first section is MLPESN approximator for the lumped unknown dynamics which will be illustrated in Sec.III.A; 2) the second section is Constrained flight control with MLPESN (including four cascade loops: trajectory, velocity, attitude, and angular rate loop), which will be illustrated in Sec.III.B. Moreover, the Lyapunov stability analysis will be presented in Sec. III.C.

It should be mentioned that the MLPESN approximators are established to accurately approximate the lumped unknown dynamics $\mathbf{F}_j$, $j = 2,3$ caused by the cable towing and airflows in the velocity and attitude loop, respectively. The aBLF based tracking controller is designed for the trajectory loop to achieve terrain obstacles avoidance. The saturations are compensated in the actuator-saturated angular rate controller. The DSC is adopted to address the "explosion of complexity".

Remark 2. This paper provides a solution to approximate the

lumped unknown dynamics $\mathbf{F}_j$, $j = 2,3$ caused by the cable towing and airflows in velocity and attitude loop, by the MLPESN approximator which not only improves the transient approximation behaviors but also decreases the online computational burden without offline training. It should be noted that the lumped unknown dynamics $\mathbf{F}_j$, $j = 2,3$ may also be estimated by suitable approaches in the framework of DOBC [21,22] or CHADC [23].
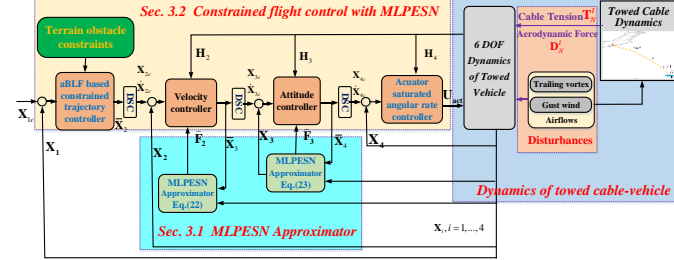

Fig. 2. The MLPESN approximator-based constrained flight controller for air-ground recovery.

A. MLPESN approximator for the major unknown dynamics

This subsection illustrates the detailed design process of the MLPESN approximator for the major unknown dynamics caused by the unmeasurable cable towing tensions and airflows in the velocity and attitude loop, as discussed in Sec. II.B.

The ESN [36-38] is a unique NN with superiority for approximating unknown system dynamics. It consists of a hidden layer with sparsely and randomly interconnected neurons and a memory-less output layer (readout). The ESN dynamics can be described as Eq. (15), with m inputs, k neurons in the hidden layer, and l neurons in the output layer.

$$\begin{cases} \dot{\mathbf{\Phi}} = C\left(-a\mathbf{\Phi} + h\left(\mathbf{W}^{in}\mathbf{u}_{in} + \mathbf{W}\mathbf{\Phi} + \mathbf{W}^{back}\mathbf{y}^{back}\right)\right) \\ \mathbf{y}^{back} = G\left(\mathbf{W}_0^T\mathbf{\Phi}\right) \end{cases} \quad (15)$$

where C and a are constants, $\mathbf{u}_{in} \in \Re^m$, $\mathbf{\Phi} \in \Re^{k\times 1}$ and $\mathbf{y}^{back} \in \Re^{l\times 1}$ are the input, state, and output vector, $h(\cdot)$ is the vector-valued nonlinear activation function, $\mathbf{W}^{in} \in \Re^{k\times m}$, $\mathbf{W} \in \Re^{k\times k}$, $\mathbf{W}^{back} \in \Re^{k\times l}$, $\mathbf{W}_0^T \in \Re^{k\times l}$ are the input-hidden, hidden-hidden, output-hidden, and hidden-output weight matrices, $G(\cdot)$ is the output activation function.

The ESN performs universal approximation [36-38] in the sense that for any given continuous function $\mathbf{F}(\cdot) \in \Re^{l\times 1}$ on a sufficiently large compact set $\Omega \in \Re$, the approximation of $\mathbf{F}(\cdot) \in \Re^{l\times 1}$ can be written as

$$\hat{\mathbf{F}}(\mathbf{u}_{in}) = \hat{\mathbf{W}}_0^T\mathbf{\Phi}, \forall \mathbf{u}_{in} \in \Omega \quad (16)$$

where $\hat{\mathbf{W}}_0$ is the estimation of $\mathbf{W}_0$. By setting $C=1$, $a=1$, $G=1$, $\dot{\mathbf{\Phi}}=0$, it derives

$$\mathbf{\Phi} = h\left(\mathbf{W}^{in}\mathbf{u}_{in} + \mathbf{W}\mathbf{\Phi} + \mathbf{W}^{back}\mathbf{y}^{back}\right) \quad (17)$$

where $\mathbf{\Phi}(\mathbf{\eta}) = \left[h_1(\mathbf{\eta}), h_2(\mathbf{\eta}),...., h_k(\mathbf{\eta})\right]^T \in \Re^k$ are Gaussian functions with the form of

$$h_j(\mathbf{\eta}) = \exp\left(-(\mathbf{\eta}-\mathbf{c}_j)^T(\mathbf{\eta}-\mathbf{c}_j)/b^2\right), j = 1,...,k \quad (18)$$

where $\mathbf{\eta} \in \Re^m$ is the input vector, b is the width of the basis function $h_j(\mathbf{\eta})$, $\mathbf{c}_j \in \Re^m$ is the center of the respective field.

For the basis function in Eq. (18), the function $\exp(\cdot)$ is strictly monotonic increasing and $-(\mathbf{\eta}-\mathbf{c}_j)^T(\mathbf{\eta}-\mathbf{c}_j)/b^2 \leq 0$, so it can be obtained that $0 < h_j(\mathbf{\eta}) \leq h_j(\mathbf{0})$. Moreover, $h_j(\mathbf{\eta})$ satisfies $h_j(\mathbf{\eta}) \leq \bar{h}$, where $\bar{h}$ is a positive constant. Furthermore, $\|\mathbf{\Phi}(\mathbf{\eta})\| \leq \hbar$, where $\hbar = k\bar{h}$.

Lemma. 1. ([36,38]). Consider an accuracy ς with a sufficiently large node number k, the ESN in Eq. (16) can approximate any unknown continuous function $\mathbf{F}(\cdot) \in \Re^{l\times 1}$ on a compact set $\Omega \in \Re$, with

$$\mathbf{F}(\mathbf{u}_{in}) = \mathbf{W}_0^{*T}\mathbf{\Phi} + \varsigma(\mathbf{u}_{in}) \quad (19)$$

where the approximation error satisfies $\|\varsigma\| \leq \varsigma_M$, ς_M is the upper bound, $\mathbf{W}_0^*$ is the ideal weight matrix of the ESN.

Based on the mapping relationship in Eq. (19), the unknown continuous function $\mathbf{F}(\mathbf{u}_{in})$ can be approximated with the ESN outputs. It should be noted that the ideal weight vector $\mathbf{W}_0^*$ is unknown and should be adaptively updated online. To reduce the computational burden of online parameter tuning dramatically, the MLP technique [38,39] is used to update the ESN weight $\mathbf{W}_0^*$ online with an adapted weight $W_0^* = \|\mathbf{W}_0^*\|^2$.

With the MLP based ESN theory above, we design the ESN approximator to identify the lumped disturbances $\mathbf{F}_i$, $i = 2,3$ in velocity and attitude loop.

For the velocity loop, the lumped unknown dynamics $\mathbf{F}_2$ can be approximated by the ESN approximator as follows

$$\begin{cases} \mathbf{F}_2 = \frac{1}{2}\mathbf{W}_{0,2}^*\mathbf{\Phi}_2^T\mathbf{\Phi}_2 + \varsigma_2 \\ \mathbf{\Phi}_2 = \left[h_{2,1}(\mathbf{\eta}_2), h_{2,2}(\mathbf{\eta}_2),..., h_{2,k}(\mathbf{\eta}_2)\right]^T \\ \mathbf{\eta}_2 = \mathbf{W}_2^{in}\mathbf{X}_2 + \mathbf{W}_2\mathbf{\Phi}_2 + \mathbf{W}_2^{back}\mathbf{y}_2^{back} \end{cases} \quad (20)$$

where $\mathbf{W}_{0,2}^* = \left[W_{Vy}^*, W_{Vz}^*\right]^T$ are the ideal ESN weights for velocity loop, and approximation error ς_2 satisfies $\|\varsigma_2\| \leq \varsigma_2^*$, $\varsigma_2^* > 0$.

The weight vector adaptive update law (21) is designed to estimate the ideal ESN weight $\mathbf{W}_{0,2}^*$.

$$\dot{\hat{\mathbf{W}}}_{0,2}^* = -\frac{\mathbf{\Gamma}_2}{2}\tilde{\mathbf{X}}_2\mathbf{\Phi}_2^T\mathbf{\Phi}_2 - \mathbf{\varphi}_2\hat{\mathbf{W}}_{0,2}^* \quad (21)$$

where $\hat{\mathbf{W}}_{0,2}^*$ is the estimation of $\mathbf{W}_{0,2}^*$, $\mathbf{\Gamma}_2 = \text{diag}\left(\Gamma_{Vy}, \Gamma_{Vz}\right)$ is the adaptive gain, $\mathbf{\varphi}_2 = \text{diag}\left(\sigma_{Vy}, \sigma_{Vz}\right)$ is a parameter to be designed, and $\tilde{\mathbf{X}}_2 = \mathbf{X}_2 - \hat{\mathbf{X}}_2$ is the state estimation error vector by the following state estimator for $\mathbf{X}_2$.

$$\begin{cases} \dot{\mathbf{X}}_2 = \dfrac{1}{2}\widehat{\mathbf{W}}_{0,2}^*\mathbf{\Phi}_2^T\mathbf{\Phi}_2 + \mathbf{H}_2 + \mathbf{B}_2\mathbf{X}_3^P + \mathbf{L}_2\tilde{\mathbf{X}}_2 \\[2mm] \widehat{\mathbf{F}}_2 = \dfrac{1}{2}\widehat{\mathbf{W}}_{0,2}^*\mathbf{\Phi}_2^T\mathbf{\Phi}_2 \end{cases} \tag{22}$$

where $\mathbf{L}_2 = \mathrm{diag}\left(L_{Vy}, L_{Vz}\right)$ is the ESN approximator parameter, and $\widehat{\mathbf{F}}_2$ is the approximation of $\mathbf{F}_2$.

Remark. 3. The weight vector adaptive update law (21) depends on the state approximation error $\tilde{\mathbf{X}}_2$ instead of the tracking error $\mathbf{e}_2$, which can decouple the design of the estimator and controller.

Similarly, the MLPESN approximator in Eq. (23) can be designed for the attitude loop to approximate $\mathbf{F}_3$.

$$\begin{cases} \mathbf{F}_3 = \dfrac{1}{2}\mathbf{W}_{0,3}^*\mathbf{\Phi}_3^T\mathbf{\Phi}_3 + \varsigma_3 \\[1mm] \mathbf{\Phi}_3 = \left[h_{3,1}(\mathbf{\eta}_3), h_{3,2}(\mathbf{\eta}_3), ..., h_{3,k}(\mathbf{\eta}_3)\right]^T \\[1mm] \mathbf{\eta}_3 = \mathbf{W}_3^{in}\mathbf{X}_3 + \mathbf{W}_3\,\mathbf{\Phi}_3 + \mathbf{W}_3^{back}\mathbf{y}_3^{back} \\[1mm] \dot{\widehat{\mathbf{W}}}_{0,3}^* = -\dfrac{\mathbf{\Gamma}_3}{2}\tilde{\mathbf{X}}_3\mathbf{\Phi}_3^T\mathbf{\Phi}_3 - \mathbf{\varphi}_3\widehat{\mathbf{W}}_{0,3}^* \\[1mm] \dot{\widehat{\mathbf{X}}}_3 = \dfrac{1}{2}\widehat{\mathbf{W}}_{0,3}^*\mathbf{\Phi}_3^T\mathbf{\Phi}_3 + \mathbf{H}_3 + \mathbf{B}_3\mathbf{X}_4 + \mathbf{L}_3\tilde{\mathbf{X}}_3 \\[1mm] \widehat{\mathbf{F}}_3 = \dfrac{1}{2}\widehat{\mathbf{W}}_{0,3}^*\mathbf{\Phi}_3^T\mathbf{\Phi}_3 \end{cases} \tag{23}$$

where $\mathbf{W}_{0,3}^* = \left[W_\alpha^*, W_\beta^*, W_\phi^*\right]^T$ are the ideal ESN weights for attitude loop, and the approximation error ς_3 satisfies $\|\varsigma_3\| \leq \varsigma_3^*$, $\varsigma_3^* > 0$; $\widehat{\mathbf{W}}_{0,3}^*$ is the estimation of $\mathbf{W}_{0,3}^*$, $\mathbf{\Gamma}_3 = \mathrm{diag}\left(\Gamma_\alpha, \Gamma_\beta, \Gamma_\phi\right)$ is the adaptive gain, $\mathbf{\varphi}_3 = \mathrm{diag}\left(\sigma_\alpha, \sigma_\beta, \sigma_\phi\right)$ is a parameter to be designed, and $\tilde{\mathbf{X}}_3 = \mathbf{X}_3 - \widehat{\mathbf{X}}_3$ is the state estimation error; $\mathbf{L}_3 = \mathrm{diag}\left(L_\alpha, L_\beta, L_\phi\right)$ is the ESN parameter, $\widehat{\mathbf{F}}_3$ is the approximation of $\mathbf{F}_3$.

B. Constrained flight control with MLPESN

With the approximation by the MLPESN approximator above, this subsection illustrates the detailed design process of the MLPESN based constrained flight controller for the air-ground recovery. The proposed MLPESN based constrained flight controller can be established with the following steps.

Step 1: The aBLF based constrained trajectory controller is established to guarantee the towed vehicle trajectory subject to the time-varying terrain obstacle constraints.

Define $\mathbf{e}_1 = \left[e_y, e_z\right]^T = \mathbf{X}_1 - \mathbf{X}_{1c}$ and $\mathbf{e}_2 = \left[e_{V_y}, e_{V_z}\right]^T = \mathbf{X}_2 - \bar{\mathbf{X}}_2$ as the trajectory and velocity tracking errors, where $\mathbf{X}_{1c} = \left[y_c, z_c\right]^T$ and $\bar{\mathbf{X}}_2 = \left[\bar{V}_{yc}, \bar{V}_{zc}\right]^T$ are the trajectory commands and velocity virtual control signal, respectively. We take the vertical trajectory z as an example to elaborate the constrained trajectory design, as the lateral trajectory channel is similar.

With the aBLF theory [15,17], the following time-varying aBLF can be designed.

$$V_z = \frac{\bar{q}(e_z)}{2\bar{p}}\log\frac{k_{b_z}^{2\bar{p}}(t)}{k_{b_z}^{2\bar{p}}(t) - e_z^{2\bar{p}}} + \frac{1 - \bar{q}(e_z)}{2\bar{p}}\log\frac{k_{a_z}^{2\bar{p}}(t)}{k_{a_z}^{2\bar{p}}(t) - e_z^{2\bar{p}}} \tag{24}$$

where $\bar{p} \geq 4/2 = 2$ is a positive integer to ensure differentiability of the virtual control signals $\bar{\mathbf{X}}_{ic}, i = 2, 3, 4$; the time-varying barriers $k_{b_z}(t), k_{a_z}(t)$ and $\bar{q}(\cdot)$ are designed as

$$k_{a_z}(t) = z_c(t) - \underline{z}_c(t) \tag{25}$$

$$k_{b_z}(t) = \bar{z}_c(t) - z_c(t) \tag{26}$$

$$\bar{q} = \bar{q}(\cdot) = \begin{cases} 1, & if\ (\cdot) > 0 \\ 0, & if\ (\cdot) \leq 0 \end{cases} \tag{27}$$

Referring to aBLF theory [17], there exist constants $\bar{k}_{a_z} > 0$, $\underline{k}_{a_z} > 0$, $\bar{k}_{b_z} > 0$ and $\underline{k}_{b_z} > 0$ satisfying

$$\underline{k}_{a_z} \leq k_{a_z}(t) \leq \bar{k}_{a_z}, \underline{k}_{b_z} \leq k_{b_z}(t) \leq \bar{k}_{b_z}, \forall t > 0 \tag{28}$$

Transfer the error coordinates with

$$\sigma_{a_z} = \frac{e_z}{k_{a_z}}, \sigma_{b_z} = \frac{e_z}{k_{b_z}}, \sigma_z = \bar{q}\sigma_{b_z} + (1 - \bar{q})\sigma_{a_z} \tag{29}$$

With the transformation, aBLF (24) can be rewritten as

$$V_z = \frac{1}{2\bar{p}}\log\frac{1}{1 - \sigma_z^{2\bar{p}}} \tag{30}$$

Thus, V_z is continuously differentiable and positive definite in the set $|\sigma_z| < 1$. Furthermore,

$$\dot{V}_z = \frac{\bar{q}\sigma_{b_z}^{2\bar{p}-1}}{k_{b_z}\left(1 - \sigma_{b_z}^{2\bar{p}}\right)}\left(\left(e_{V_z} + \bar{V}_{zc}\right) - \dot{z}_c - e_z\frac{\dot{k}_{b_z}}{k_{b_z}}\right)$$
$$+ \frac{(1 - \bar{q})\sigma_{a_z}^{2\bar{p}-1}}{k_{a_z}\left(1 - \sigma_{a_z}^{2\bar{p}}\right)}\left(\left(e_{V_z} + \bar{V}_{zc}\right) - \dot{z}_c - e_z\frac{\dot{k}_{a_z}}{k_{a_z}}\right) \tag{31}$$

Then, the following aBLF based control law for the vertical trajectory channel is designed.

$$\begin{cases} \bar{V}_{zc} = -\left(\kappa_z + \bar{\kappa}_z(t)\right)e_z + \dot{z}_c \\[2mm] \bar{\kappa}_z(t) = \sqrt{\left(\dfrac{\dot{k}_{a_z}}{k_{a_z}}\right)^2 + \left(\dfrac{\dot{k}_{b_z}}{k_{b_z}}\right)^2} + \rho_z \end{cases} \tag{32}$$

where κ_z is the constant control gain, $\bar{\kappa}_z(t)$ is the time-varying gain, positive constant ρ_z guarantees the boundedness of $\dot{\bar{V}}_{zc}$ even when $\dot{k}_{a_z}$ and $\dot{k}_{b_z}$ are both zero.

By selecting aBLF with the same form of Eq. (24), the aBLF based lateral trajectory control law is similarly designed.

$$\begin{cases} \bar{V}_{yc} = -\left(\kappa_y + \bar{\kappa}_y(t)\right)e_y + \dot{y}_c \\[2mm] \bar{\kappa}_y(t) = \sqrt{\left(\dfrac{\dot{k}_{a_y}}{k_{a_y}}\right)^2 + \left(\dfrac{\dot{k}_{b_y}}{k_{b_y}}\right)^2} + \rho_y \end{cases} \tag{33}$$

where κ_y is the constant control gain, $\bar{\kappa}_y(t)$ is the time-varying gain, ρ_z is a positive constant, $k_{a_y}(t) = y_c(t) - \underline{y}_c(t)$, $k_{b_y}(t) = \bar{y}_c(t) - y_c(t)$.

Therefore, the constrained trajectory control law can be obtained with Eqs. (32) and (33).

$$\bar{\mathbf{X}}_2 = \left[\bar{V}_{yc}, \bar{V}_{zc}\right]^T \tag{34}$$

To handle the "explosion of complexity" in backstepping,

the DSC (35) with a time constant $\tau_2 > 0$ is used to get the command $\mathbf{X}_{2c}$ and its derivative for the velocity loop [18-20].

$$\tau_2 \dot{\mathbf{X}}_{2c} + \mathbf{X}_{2c} = \bar{\mathbf{X}}_2 - \tau_2 \boldsymbol{\mu}_1 \mathbf{e}_1^{2\bar{p}-1}, \mathbf{X}_{2c}(0) = \bar{\mathbf{X}}_2(0) \quad (35)$$

By defining $\boldsymbol{\varepsilon}_2 = \left[\varepsilon_y, \varepsilon_z\right]^T = \mathbf{X}_{2c} - \bar{\mathbf{X}}_2$ as the filtering error, with control law in Eq. (34), its derivative can be derived

$$
\begin{aligned}
\dot{\boldsymbol{\varepsilon}}_2 &= -\frac{1}{\tau_2}\boldsymbol{\varepsilon}_2 - \dot{\bar{\mathbf{X}}}_{2c} - \boldsymbol{\mu}_1 \mathbf{e}_1^{2\bar{p}-1} \\
&= -\frac{1}{\tau_2}\boldsymbol{\varepsilon}_2 - \frac{d\left(-\left(\boldsymbol{\kappa}_1 + \bar{\boldsymbol{\kappa}}_1(t)\right)\mathbf{e}_1 + \dot{\mathbf{X}}_{1c}\right)}{dt} - \boldsymbol{\mu}_1 \mathbf{e}_1^{2\bar{p}-1} \quad (36) \\
&= -\frac{1}{\tau_2}\boldsymbol{\varepsilon}_2 - \boldsymbol{\mu}_1 \mathbf{e}_1^{2\bar{p}-1} + M_1\left(\mathbf{B}_1, \mathbf{e}_1, \dot{\mathbf{X}}_{1c}\right)
\end{aligned}
$$

where $M_1\left(\mathbf{B}_1, \mathbf{e}_1, \dot{\mathbf{X}}_{1c}\right) = -d\left(-\left(\boldsymbol{\kappa}_1 + \bar{\boldsymbol{\kappa}}_1(t)\right)\mathbf{e}_1 + \dot{\mathbf{X}}_{1c}\right)/dt$,
$\boldsymbol{\kappa}_1 = \mathrm{diag}\left(\kappa_y, \kappa_z\right)$, $\bar{\boldsymbol{\kappa}}_1(t) = \mathrm{diag}\left(\bar{\kappa}_y(t), \bar{\kappa}_z(t)\right)$.

Remark. 4. According to Swaroop *et al.* [18], for filtering the error dynamics $\dot{\boldsymbol{\varepsilon}}_2$, there exists a maximum constant $M_{1\max} > 0$ such that $\|M_1\| \leq M_{1\max}$.

Furthermore, with Eqs. (29), (31), and (32), we get the following inequality.

$$
\begin{aligned}
\dot{V}_z &\leq -\frac{\kappa_z \sigma_z^{2\bar{p}}}{1-\sigma_z^{2\bar{p}}} + \underbrace{\left(\frac{\bar{q}}{k_{b_z}^{2\bar{p}}-e_z^{2\bar{p}}} + \frac{1-\bar{q}}{k_{a_z}^{2\bar{p}}-e_z^{2\bar{p}}}\right)}_{\mu_z} e_z^{2\bar{p}-1}\left(e_{V_z} + \varepsilon_z\right) \quad (37) \\
&= -\frac{\kappa_z \sigma_{b_z}^{2\bar{p}}}{1-\sigma_{b_z}^{2\bar{p}}} + \mu_z e_z^{2\bar{p}-1}\left(e_{V_z} + \varepsilon_z\right)
\end{aligned}
$$

Similarly,

$$
\begin{aligned}
\dot{V}_y &\leq -\frac{\kappa_y \sigma_{b_y}^{2\bar{p}}}{1-\sigma_{b_y}^{2\bar{p}}} + \underbrace{\left(\frac{\bar{q}}{k_{b_y}^{2\bar{p}}-e_y^{2\bar{p}}} + \frac{1-\bar{q}}{k_{a_y}^{2\bar{p}}-e_y^{2\bar{p}}}\right)}_{\mu_y} e_y^{2\bar{p}-1}\left(e_{V_y} + \varepsilon_y\right) \quad (38) \\
&= -\frac{\kappa_y \sigma_{b_y}^{2\bar{p}}}{1-\sigma_{b_y}^{2\bar{p}}} + \mu_y e_y^{2\bar{p}-1}\left(e_{V_y} + \varepsilon_y\right)
\end{aligned}
$$

Step 2: Define velocity tracking error $\mathbf{e}_2 = \left[e_{Vy}, e_{Vz}\right]^T = \mathbf{X}_2 - \mathbf{X}_{2c}$, we get

$$\dot{\mathbf{e}}_2 = \dot{\mathbf{X}}_2 - \dot{\mathbf{X}}_{2c} = \mathbf{F}_2 + \mathbf{B}_2 \mathbf{X}_3^P - \dot{\mathbf{X}}_{2c} \quad (39)$$

According to aBLF based backstepping [17], we design the velocity control law

$$
\begin{cases}
\bar{\mathbf{X}}_3^P = \left[\bar{\beta}, \bar{\alpha}\right]^T = \mathbf{B}_2^{-1}\left(-\mathbf{H}_2 - \hat{\mathbf{F}}_2 - \boldsymbol{\kappa}_2 \mathbf{e}_2 + \dot{\mathbf{X}}_{2c} - \boldsymbol{\mu}_1 \mathbf{e}_1^{2\bar{p}-1}\right) \\
\boldsymbol{\mu}_1 = \mathrm{diag}\left(\mu_y, \mu_z\right)
\end{cases}
$$
$$(40)$$

where $\boldsymbol{\kappa}_2 > 0$ is the control gain, $\hat{\mathbf{F}}_2$ is the approximation of the lumped disturbance $\mathbf{F}_2$ by MLP based ESN approximators (20)-(22); $-\boldsymbol{\mu}_1 \mathbf{B}_1^T \mathbf{e}_1^{2\bar{p}-1}$ is included to compensate for the trajectory tracking residual error, which will be used in the later stability analysis.

To address the explosion of complexity, the DSC in Eq. (41) with a time constant $\tau_3 > 0$ is designed to get the command $\mathbf{X}_{3c}^P$ and its derivative for the attitude loop.

$$\tau_3 \dot{\mathbf{X}}_{3c}^P + \mathbf{X}_{3c}^P = \bar{\mathbf{X}}_3^P - \tau_3 \mathbf{B}_2^T \mathbf{e}_2, \mathbf{X}_{3c}^P(0) = \bar{\mathbf{X}}_3^P(0) \quad (41)$$

The derivative of the filtering error $\boldsymbol{\varepsilon}_3 = \mathbf{X}_{3c}^P - \bar{\mathbf{X}}_3^P$ can be obtained as

$$
\begin{aligned}
\dot{\boldsymbol{\varepsilon}}_3 &= -\frac{1}{\tau_3}\boldsymbol{\varepsilon}_3 - \dot{\bar{\mathbf{X}}}_3^P - \mathbf{B}_2^T \mathbf{e}_2 \\
&= -\frac{1}{\tau_3}\boldsymbol{\varepsilon}_3 - \mathbf{B}_2^T \mathbf{e}_2 + M_2\left(\mathbf{B}_1, \mathbf{B}_2, \mathbf{e}_1, \mathbf{e}_2, \dot{\mathbf{X}}_{2c}, \hat{\mathbf{F}}_2\right)
\end{aligned} \quad (42)
$$

where $M_2\left(\mathbf{B}_1, \mathbf{B}_2, \mathbf{e}_1, \mathbf{e}_2, \dot{\mathbf{X}}_{2c}, \hat{\mathbf{F}}_2\right) = -d\left(-\hat{\mathbf{F}}_2 - \boldsymbol{\kappa}_2 \mathbf{e}_2 + \dot{\mathbf{X}}_{2c} - \boldsymbol{\mu}_1 \mathbf{B}_1^T \mathbf{e}_1^{2\bar{p}-1}\right)/dt$.

Step 3: Define the attitude tracking errors $\mathbf{e}_3 = \mathbf{X}_3 - \mathbf{X}_{3c}$, where $\mathbf{X}_{3c} = \left[0, \mathbf{X}_{3c}^P(1), \mathbf{X}_{3c}^P(2)\right]^T$ is the command signal. Then, the attitude control law can be designed as

$$\bar{\mathbf{X}}_4 = \mathbf{B}_3^{-1}\left(-\mathbf{H}_3 - \hat{\mathbf{F}}_3 - \boldsymbol{\kappa}_3 \mathbf{e}_3 + \dot{\mathbf{X}}_{3c} - \mathbf{B}_2^T \mathbf{e}_2\right) \quad (43)$$

where $\boldsymbol{\kappa}_3 > 0$ is the control gain, $\hat{\mathbf{F}}_3$ is the approximation of the lumped disturbance by the ESN approximator (23).

Similarly, the DSC in Eq. (44) with a time constant $\tau_4 > 0$ is designed to the command $\mathbf{X}_{4c}$ for the angular rate loop with the virtual control signal $\bar{\mathbf{X}}_4$.

$$\tau_4 \dot{\mathbf{X}}_{4c} + \mathbf{X}_{4c} = \bar{\mathbf{X}}_4 - \tau_4 \mathbf{B}_3^T \mathbf{e}_3, \mathbf{X}_{4c}(0) = \bar{\mathbf{X}}_4(0) \quad (44)$$

The derivative of filtering error $\boldsymbol{\varepsilon}_4 = \mathbf{X}_{4c} - \bar{\mathbf{X}}_4$ is derived:

$$
\begin{aligned}
\dot{\boldsymbol{\varepsilon}}_4 &= -\frac{1}{\tau_4}\boldsymbol{\varepsilon}_4 - \dot{\bar{\mathbf{X}}}_4 - \mathbf{B}_3^T \mathbf{e}_3 \\
&= -\frac{1}{\tau_4}\boldsymbol{\varepsilon}_4 - \mathbf{B}_3^T \mathbf{e}_3 + M_3\left(\mathbf{B}_2, \mathbf{B}_3, \mathbf{e}_2, \mathbf{e}_3, \dot{\mathbf{X}}_{3c}, \hat{\mathbf{F}}_3\right)
\end{aligned} \quad (45)
$$

where $M_3\left(\mathbf{B}_2, \mathbf{B}_3, \mathbf{e}_2, \mathbf{e}_3, \dot{\mathbf{X}}_{3c}, \hat{\mathbf{F}}_3\right) = -d\left(\mathbf{B}_3^{-1}\left(-\hat{\mathbf{F}}_3 - \boldsymbol{\kappa}_3 \mathbf{e}_3 + \dot{\mathbf{X}}_{3c} - \mathbf{B}_2^T \mathbf{e}_2\right)\right)/dt$.

Step 4: Define the angle tracking error vector $\mathbf{e}_4 = \mathbf{X}_4 - \mathbf{X}_{4c}$.

Considering that the actuator inputs $\mathbf{U}_{act} = \left[\delta_a, \delta_e, \delta_r\right]^T$ may be saturated, the saturation compensation and exiting mechanism should be considered during the angle rate control law design [42-43,45,47]. To cope with the actuator saturation effect, the following auxiliary system Eq. (46) can be established for the saturation compensation of angular rate control law [47].

$$\dot{\boldsymbol{\chi}} = -\frac{\boldsymbol{\Psi}\boldsymbol{\chi}}{\|\boldsymbol{\chi}\| + \delta} + \mathbf{B}_4\left(\mathbf{U}_{act} - \bar{\mathbf{U}}_{act}\right) \quad (46)$$

where $\boldsymbol{\chi}$ is the auxiliary system state, $\boldsymbol{\Psi}$ and δ are the constant parameters to be designed, $\mathbf{U}_{act}$ is the actual output of the saturated actuator, $\bar{\mathbf{U}}_{act}$ is the command of the actuator generated by the angular rate control law designed below. And there exists $\bar{U}$ satisfying $\bar{U} \geq \left|\mathbf{U}_{act} - \bar{\mathbf{U}}_{act}\right|$.

Define an additional error $\mathbf{E}_4 = \mathbf{e}_4 - \boldsymbol{\chi}$, we get the derivative of $\mathbf{E}_4$.

$$\dot{\mathbf{E}}_4 = \mathbf{F}_4 + \mathbf{B}_4 \mathbf{U}_{act} - \dot{\mathbf{X}}_{4c} + \frac{\boldsymbol{\Psi}\boldsymbol{\chi}}{\|\boldsymbol{\chi}\| + \delta} - \mathbf{B}_4\left(\mathbf{U}_{act} - \bar{\mathbf{U}}_{act}\right) \quad (47)$$

Consequently, with the established auxiliary compensating system Eq. (46), the desired angular rate control law considering actuator saturation can be designed as

$$\bar{\mathbf{U}}_{act} = \mathbf{B}_4^{-1}\left(-\mathbf{H}_4 - \boldsymbol{\kappa}_4 \mathbf{E}_4 + \dot{\mathbf{X}}_{4c} - \mathbf{B}_3^T \mathbf{e}_3 - \frac{\boldsymbol{\Psi}\boldsymbol{\chi}}{\|\boldsymbol{\chi}\| + \delta}\right) \quad (48)$$

This article has been accepted for publication in a future issue of this journal, but has not been fully edited. Content may change prior to final publication. Citation information: DOI 10.1109/TAES.2021.3101592, IEEE Transactions on Aerospace and Electronic Systems

> REPLACE THIS LINE WITH YOUR PAPER IDENTIFICATION NUMBER (DOUBLE-CLICK HERE TO EDIT) < 9

where κ_4 is the control gain.

Remark 5. Compared with the traditional backstepping-based control law [6,20,26-27], the extra $-\dfrac{\mathbf{\Psi}\boldsymbol{\chi}}{\|\boldsymbol{\chi}\|+\delta}$ is included in the angle rate control law Eq. (48) for actuator saturation compensation. When the actuator saturations occur, $-\dfrac{\mathbf{\Psi}\boldsymbol{\chi}}{\|\boldsymbol{\chi}\|+\delta}$ will guide the control law to exist the saturation.

C. Closed-loop stability analysis

This subsection mainly discusses the closed stability of the MLPESN based constrained flight control system established in Sec. III.A and III.B. The Lyapunov stability can be concluded with Theorem 1 below.

Theorem. 1. Considering the dynamics (6)-(9), the proposed constrained flight controller consisting of the control laws (34), (40), (43), (48), DSC (35), (41), (44), and MLP based ESN approximators (22), (23), there exist parameters κ_y, κ_z , $\kappa_i, i=1,2,3,4$, $\mathbf{\Phi}$, $\tau_i, \mathbf{L}_i, \mathbf{\Gamma}_i, \boldsymbol{\varphi}_i, i=2,3,4$ satisfying Eq. (49), such that the uniformly ultimately bounded stability of the closed-loop system can be ensured and the towed vehicle's trajectory $\mathbf{X}_1$ will never violate terrain constraints (12)-(13).

$$\kappa_y > 0, \kappa_z > 0, \pi_{12} = \lambda_{\min}(\kappa_2) - \frac{h^2}{4} - \frac{1}{2} > 0,$$

$$\pi_{13} = \lambda_{\min}(\kappa_3) - \frac{\lambda_{\max}(\mathbf{B}_3)}{2} - \frac{h^2}{4} - \frac{1}{2} > 0,$$

$$\pi_{14} = \lambda_{\min}(\kappa_4) > 0,$$

$$\pi_2 = \frac{\lambda_{\min}(\mathbf{\Phi})}{\|\boldsymbol{\chi}\|+\delta} - \frac{\lambda_{\max}(\mathbf{B}_3)}{2} - \lambda_{\max}(\mathbf{B}_4)\bar{\mathbf{U}} > 0,$$

$$\pi_{3i} = \frac{1}{\tau_i} - \frac{1}{2} > 0, i = 2,3,4 \tag{49}$$

$$\pi_{4j} = \lambda_{\min}(\mathbf{L}_j) - \frac{h^2}{4} - \frac{1}{2} - \frac{h^2}{2}\lambda_{\max}(\mathbf{\Gamma}_j) > 0,$$

$$\pi_{5j} = \frac{\lambda_{\min}(\boldsymbol{\varphi}_j) - h^2\lambda_{\max}(\mathbf{\Gamma}_j) - \lambda_{\max}(\boldsymbol{\varphi}_j) - h^2}{2} > 0,$$

$$j = 2,3$$

Proof. Consider the following Lyapunov function candidate

$$\begin{cases} V = V_1 + V_2 + V_3 + V_4 + V_5 \\ V_1 = V_y + V_z + \frac{1}{2}\mathbf{e}_2^{\mathrm{T}}\mathbf{e}_2 + \frac{1}{2}\mathbf{e}_3^{\mathrm{T}}\mathbf{e}_3 + \frac{1}{2}\mathbf{E}_4^{\mathrm{T}}\mathbf{E}_4 \\ V_2 = \frac{1}{2}\boldsymbol{\chi}^{\mathrm{T}}\boldsymbol{\chi} \\ V_3 = \sum_{i=2}^4 \frac{1}{2}\boldsymbol{\varepsilon}_{i+1}^{\mathrm{T}}\boldsymbol{\varepsilon}_{i+1} \\ V_4 = \sum_{i=2}^3 \frac{1}{2}\tilde{\mathbf{X}}_i^{\mathrm{T}}\tilde{\mathbf{X}}_i \\ V_5 = \sum_{i=2}^3 \frac{1}{2}\tilde{\mathbf{W}}_{0,i}^{*\mathrm{T}}\mathbf{\Gamma}_i^{-1}\tilde{\mathbf{W}}_{0,i}^* \end{cases} \tag{50}$$

The tracking errors $\mathbf{e}_2, \mathbf{e}_3$, $\mathbf{E}_4$, estimation errors $\tilde{\mathbf{X}}_i, \tilde{\mathbf{W}}_i, \tilde{\mathbf{F}}_i = \mathbf{F}_i - \hat{\mathbf{F}}_i, i=2,3$, and filtering errors $\boldsymbol{\varepsilon}_i, i=2,3,4$ should all be considered for the stability analysis. The derivatives of these errors should be derived before the stability analysis.

By recalling $\boldsymbol{\varepsilon}_3 = \mathbf{X}_{3c}^P - \bar{\mathbf{X}}_3^P, \mathbf{e}_2 = \mathbf{X}_3^P - \mathbf{X}_{3c}^P$ and control law in Eq. (40), it derives

$$\dot{\mathbf{e}}_2 = -\kappa_2\mathbf{e}_2 + \mathbf{B}_2\left(\mathbf{e}_3^P + \boldsymbol{\varepsilon}_3\right) + \tilde{\mathbf{F}}_2 - \mu_1\mathbf{e}_1^{2\bar{p}-1}$$
$$\mathbf{e}_3^P = \left[\mathbf{e}_3(1), \mathbf{e}_3(2)\right]^{\mathrm{T}} \tag{51}$$

Similarly, it derives

$$\begin{cases} \dot{\mathbf{e}}_3 = -\kappa_3\mathbf{e}_3 + \mathbf{B}_3\left(\mathbf{e}_4 + \boldsymbol{\varepsilon}_4\right) + \tilde{\mathbf{F}}_3 - \left[0, \mathbf{H}(1), \mathbf{H}(2)\right]^T \\ \mathbf{H} = \mathbf{B}_2^{\mathrm{T}}\mathbf{e}_2 \end{cases} \tag{52}$$

With Eq. (48) and control law (49), we get the derivative of $\mathbf{E}_4$ as

$$\dot{\mathbf{E}}_4 = \mathbf{H}_4 - \dot{\mathbf{X}}_{4c} + \frac{\mathbf{\Phi}\boldsymbol{\chi}}{\|\boldsymbol{\chi}\|+\delta} + \mathbf{B}_4\mathbf{B}_4^{-1}\begin{pmatrix} -\mathbf{H}_4 - \kappa_4\mathbf{E}_4 + \dot{\mathbf{X}}_{4c} - \\ \mathbf{B}_3^{\mathrm{T}}\mathbf{e}_3 - \dfrac{\mathbf{\Phi}\boldsymbol{\chi}}{\|\boldsymbol{\chi}\|+\delta} \end{pmatrix} \tag{53}$$

$$= -\kappa_4\mathbf{E}_4 - \mathbf{B}_3^{\mathrm{T}}\mathbf{e}_3$$

By recalling the formulation of the MLPESN approximator, we obtain $\tilde{\mathbf{F}}_i = \mathbf{F}_i - \hat{\mathbf{F}}_i, i=2,3$ and the derivatives of the approximation errors $\tilde{\mathbf{X}}_i = \mathbf{X}_i - \hat{\mathbf{X}}_i, \tilde{\mathbf{W}}_{0,i}^* = \mathbf{W}_{0,i}^* - \hat{\mathbf{W}}_{0,i}^*, i=2,3$.

$$\tilde{\mathbf{F}}_i = -\frac{1}{2}\tilde{\mathbf{W}}_{0,i}^*\left\|\mathbf{\Phi}_i\left(\boldsymbol{\eta}_i\right)\right\|^2 + \varsigma_i, i=2,3 \tag{54}$$

$$\dot{\tilde{\mathbf{X}}}_i = -\mathbf{L}_i\tilde{\mathbf{X}}_i + \frac{1}{2}\tilde{\mathbf{W}}_{0,i}^*\left\|\mathbf{\Phi}_i\left(\boldsymbol{\eta}_i\right)\right\|^2 - \varsigma_i, i=2,3 \tag{55}$$

$$\dot{\tilde{\mathbf{W}}}_{0,i}^* = \frac{\mathbf{\Gamma}_i}{2}\tilde{\mathbf{X}}_i\left\|\mathbf{\Phi}_i\left(\boldsymbol{\eta}_i\right)\right\|^2 + \boldsymbol{\varphi}_i\hat{\mathbf{W}}_{0,i}^*, i=2,3 \tag{56}$$

Differentiating Eq. (50) to time yields

$$\dot{V}_1 = -\dot{V}_y - \dot{V}_z - \mathbf{e}_2^{\mathrm{T}}\kappa_2\mathbf{e}_2 - \mathbf{e}_3^{\mathrm{T}}\kappa_3\mathbf{e}_3 - \mathbf{E}_4^{\mathrm{T}}\kappa_4\mathbf{E}_4$$
$$+ \mathbf{e}_3^{\mathrm{T}}\mathbf{B}_3\boldsymbol{\chi} + \mathbf{e}_2^{\mathrm{T}}\mu_1\mathbf{e}_1^{2\bar{p}-1}$$
$$+ \mathbf{e}_2^{\mathrm{T}}\mathbf{B}_2\boldsymbol{\varepsilon}_3 + \mathbf{e}_3^{\mathrm{T}}\mathbf{B}_3\boldsymbol{\varepsilon}_4 \tag{57}$$
$$+ \mathbf{e}_2^{\mathrm{T}}\tilde{\mathbf{F}}_2 + \mathbf{e}_3^{\mathrm{T}}\tilde{\mathbf{F}}_3$$

$$\dot{V}_2 = \boldsymbol{\chi}^{\mathrm{T}}\left(-\frac{\mathbf{\Psi}\boldsymbol{\chi}}{\|\boldsymbol{\chi}\|+\delta} + \mathbf{B}_4\left(\mathbf{U}_{\mathrm{act}} - \bar{\mathbf{U}}_{\mathrm{act}}\right)\right)$$
$$= -\frac{\boldsymbol{\chi}^{\mathrm{T}}\mathbf{\Psi}\boldsymbol{\chi}}{\|\boldsymbol{\chi}\|+\delta} + \boldsymbol{\chi}^{\mathrm{T}}\mathbf{B}_4\left(\mathbf{U}_{\mathrm{act}} - \bar{\mathbf{U}}_{\mathrm{act}}\right) \tag{58}$$

$$\dot{V}_3 = \sum_{i=2}^4 \frac{1}{2}\boldsymbol{\varepsilon}_{i+1}^{\mathrm{T}}\dot{\boldsymbol{\varepsilon}}_{i+1}$$
$$= -\sum_{i=2}^3 \frac{1}{\tau_i}\boldsymbol{\varepsilon}_i^{\mathrm{T}}\boldsymbol{\varepsilon}_i - \sum_{i=2}^3 \boldsymbol{\varepsilon}_i^{\mathrm{T}}\mathbf{B}_{i-1}^{\mathrm{T}}\mathbf{e}_{i-1} + \sum_{i=2}^3 \boldsymbol{\varepsilon}_i^{\mathrm{T}}\mathbf{M}_i \tag{59}$$

$$\dot{V}_4 = \sum_{i=2}^3 \frac{1}{2}\tilde{\mathbf{X}}_i^{\mathrm{T}}\tilde{\mathbf{X}}_i = -\sum_{i=2}^3 \tilde{\mathbf{X}}_i^{\mathrm{T}}\mathbf{L}_i\tilde{\mathbf{X}}_i$$
$$+ \sum_{i=2}^3 \frac{1}{2}\tilde{\mathbf{X}}_i^{\mathrm{T}}\tilde{\mathbf{W}}_{0,i}^*\left\|\mathbf{\Phi}_i\left(\boldsymbol{\eta}_i\right)\right\|^2 - \sum_{i=2}^3 \tilde{\mathbf{X}}_i^{\mathrm{T}}\varsigma_i \tag{60}$$

This article has been accepted for publication in a future issue of this journal, but has not been fully edited. Content may change prior to final publication. Citation information: DOI 10.1109/TAES.2021.3101592, IEEE Transactions on Aerospace and Electronic Systems

> REPLACE THIS LINE WITH YOUR PAPER IDENTIFICATION NUMBER (DOUBLE-CLICK HERE TO EDIT) <   10

$$\dot{V}_5 = \sum_{i=2}^{3} \frac{1}{2} \tilde{\mathbf{W}}_{0,i}^{*\mathrm{T}} \Gamma_i^{-1} \dot{\tilde{\mathbf{W}}}_{0,i}^{*}$$
$$= -\sum_{i=2}^{3} \frac{1}{2} \left(\tilde{\mathbf{W}}_{0,i}^{*\mathrm{T}} \left\| \boldsymbol{\Phi}_i (\boldsymbol{\eta}_i) \right\|^2 \tilde{\mathbf{X}}_i + \tilde{\mathbf{W}}_{0,i}^{*\mathrm{T}} \boldsymbol{\varphi}_i \hat{\mathbf{W}}_{0,i}^{*} \right) \quad (61)$$

According to Young's inequality [25], we derive the following inequalities.

$$-\mathbf{e}_i^{\mathrm{T}} \boldsymbol{\kappa}_i \mathbf{e}_i \le -\lambda_{\min} (\boldsymbol{\kappa}_i) \left\| \mathbf{e}_i \right\|^2, i = 2,3 \quad (62)$$

$$-\mathbf{E}_4^{\mathrm{T}} \boldsymbol{\kappa}_4 \mathbf{E}_4 \le -\lambda_{\min} (\boldsymbol{\kappa}_4) \left\| \mathbf{E}_4 \right\|^2 \quad (63)$$

$$\mathbf{e}_3^{\mathrm{T}} \mathbf{B}_3 \boldsymbol{\chi} \le \lambda_{\max} (\mathbf{B}_3) \left\| \mathbf{e}_3 \right\| \left\| \boldsymbol{\chi} \right\|$$
$$\le \frac{\lambda_{\max} (\mathbf{B}_3)}{2} \left\| \mathbf{e}_3 \right\|^2 + \frac{\lambda_{\max} (\mathbf{B}_3)}{2} \left\| \boldsymbol{\chi} \right\| \quad (64)$$

$$\mathbf{e}_i^{\mathrm{T}} \tilde{\mathbf{F}}_i \le \mathbf{e}_i^{\mathrm{T}} \left(-\frac{1}{2} \tilde{\mathbf{W}}_{0,i}^{*} \left\| \boldsymbol{\Phi}_i (\boldsymbol{\eta}_i) \right\|^2 + \varsigma_i \right)$$
$$\le \frac{\hbar^2}{4} \left\| \mathbf{e}_i \right\|^2 + \frac{\hbar^2}{4} \left\| \tilde{\mathbf{W}}_{0,i}^{*} \right\|^2 + \frac{1}{2} \left\| \mathbf{e}_i \right\|^2 + \frac{1}{2} \varsigma_i^{*2}, i = 2,3 \quad (65)$$

$$-\frac{\boldsymbol{\chi}^{\mathrm{T}} \boldsymbol{\Psi} \boldsymbol{\chi}}{\left\| \boldsymbol{\chi} \right\| + \delta} \le -\frac{\lambda_{\min} (\boldsymbol{\Psi}) \left\| \boldsymbol{\chi} \right\|^2}{\left\| \boldsymbol{\chi} \right\| + \delta} \quad (66)$$

$$-\sum_{i=2}^{4} \frac{1}{\tau_i} \boldsymbol{\varepsilon}_i^{\mathrm{T}} \boldsymbol{\varepsilon}_i \le -\sum_{i=2}^{4} \frac{1}{\tau_i} \left\| \boldsymbol{\varepsilon}_{i+1} \right\|^2 \quad (67)$$

$$\sum_{i=2}^{4} \boldsymbol{\varepsilon}_i^{\mathrm{T}} M_i \le \sum_{i=2}^{4} \left\| \boldsymbol{\varepsilon}_i \right\| \left\| M_i \right\|$$
$$\le \sum_{i=2}^{4} \frac{1}{2} \left\| \boldsymbol{\varepsilon}_{i+1} \right\|^2 + \sum_{i=2}^{4} \frac{1}{2} M_{i,\max}^2 \quad (68)$$

$$-\sum_{i=2}^{4} \tilde{\mathbf{X}}_i^{\mathrm{T}} \mathbf{L}_i \tilde{\mathbf{X}}_i \le -\sum_{i=2}^{4} \lambda_{\min} (\mathbf{L}_i) \left\| \tilde{\mathbf{X}}_i \right\|^2 \quad (69)$$

$$\sum_{i=2}^{3} \frac{1}{2} \tilde{\mathbf{X}}_i^{\mathrm{T}} \tilde{\mathbf{W}}_{0,i}^{*} \left\| \boldsymbol{\Phi}_i (\boldsymbol{\eta}_i) \right\|^2 \le \sum_{i=2}^{3} \frac{\hbar^2}{4} \left\| \tilde{\mathbf{X}}_i \right\|^2 + \sum_{i=2}^{3} \frac{\hbar^2}{4} \left\| \tilde{\mathbf{W}}_{0,i}^{*} \right\|^2 \quad (70)$$

$$-\sum_{i=2}^{3} \tilde{\mathbf{X}}_i^{\mathrm{T}} \varsigma_i \le \sum_{i=2}^{3} \left\| \tilde{\mathbf{X}}_i \right\| \left\| \varsigma_i \right\|$$
$$\le \sum_{i=2}^{3} \frac{1}{2} \left\| \tilde{\mathbf{X}}_i \right\|^2 + \sum_{i=2}^{4} \frac{1}{2} \varsigma_i^{*2} \quad (71)$$

$$-\sum_{i=2}^{3} \left(\tilde{\mathbf{W}}_{0,i}^{*\mathrm{T}} \frac{\Gamma_i}{2} \left\| \boldsymbol{\Phi}_i (\boldsymbol{\eta}_i) \right\|^2 \tilde{\mathbf{X}}_i + \tilde{\mathbf{W}}_{0,i}^{*\mathrm{T}} \boldsymbol{\varphi}_i \hat{\mathbf{W}}_{0,i}^{*} \right)$$
$$\le \sum_{i=2}^{3} \left(\begin{array}{c} \frac{\hbar^2}{2} \lambda_{\max} (\Gamma_i) \left\| \tilde{\mathbf{X}}_i \right\|^2 + \frac{\lambda_{\max} (\boldsymbol{\varphi}_i)}{2} \Upsilon^2 + \\ \frac{\hbar^2 \lambda_{\max} (\Gamma_i) - \lambda_{\min} (\boldsymbol{\varphi}_i) + \lambda_{\max} (\boldsymbol{\varphi}_i)}{2} \left\| \tilde{\mathbf{W}}_{0,i}^{*} \right\|^2 \end{array} \right) \quad (72)$$

$$\boldsymbol{\chi}^{\mathrm{T}} \mathbf{B}_4 \left(\mathbf{U}_{\mathrm{act}} - \bar{\mathbf{U}}_{\mathrm{act}} \right) \le \lambda_{\max} (\mathbf{B}_4) \bar{U} \left\| \boldsymbol{\chi} \right\|^2 \quad (73)$$

where $\lambda_{\min} (\bullet)$ and $\lambda_{\max} (\bullet)$ are the minimum and maximum eigenvalues of a matrix; $\Upsilon^2 = \max \left\{ W_j^*, j = V_y, V_z, \beta, \alpha, \phi, p, q, r \right\}$.

Then, the following inequality can be further derived.

$$\dot{V} \le -\frac{\kappa_y \sigma_{b_y}^{2\bar{p}}}{1 - \sigma_{b_y}^{2\bar{p}}} - \frac{\kappa_z \sigma_{b_z}^{2\bar{p}}}{1 - \sigma_{b_z}^{2\bar{p}}} - \lambda_{\min} (\boldsymbol{\kappa}_2) \left\| \mathbf{e}_2 \right\|^2 - \lambda_{\min} (\boldsymbol{\kappa}_3) \left\| \mathbf{e}_3 \right\|^2$$
$$- \lambda_{\min} (\boldsymbol{\kappa}_4) \left\| \mathbf{E}_4 \right\|^2 + \frac{\lambda_{\max} (\mathbf{B}_3)}{2} \left\| \mathbf{e}_3 \right\|^2 + \frac{\lambda_{\max} (\mathbf{B}_3)}{2} \left\| \boldsymbol{\chi} \right\|^2$$
$$+ \frac{\hbar^2}{4} \left\| \mathbf{e}_2 \right\|^2 + \frac{\hbar^2}{4} \left\| \tilde{\mathbf{W}}_{0,2}^{*} \right\|^2 + \frac{1}{2} \left\| \mathbf{e}_2 \right\|^2 + \frac{1}{2} \varsigma_2^{*2} + \frac{\hbar^2}{4} \left\| \mathbf{e}_3 \right\|^2$$
$$+ \frac{\hbar^2}{4} \left\| \tilde{\mathbf{W}}_{0,3}^{*} \right\|^2 + \frac{1}{2} \left\| \mathbf{e}_3 \right\|^2 + \frac{1}{2} \varsigma_3^{*2} - \frac{\lambda_{\min} (\boldsymbol{\Psi}) \left\| \boldsymbol{\chi} \right\|^2}{\left\| \boldsymbol{\chi} \right\| + \delta}$$
$$+ \lambda_{\max} (\mathbf{B}_4) \bar{U} \left\| \boldsymbol{\chi} \right\|^2 - \sum_{i=2}^{4} \frac{1}{\tau_i} \left\| \boldsymbol{\varepsilon}_i \right\|^2 + \sum_{i=2}^{4} \frac{1}{2} \left\| \boldsymbol{\varepsilon}_{i+1} \right\|^2$$
$$+ \sum_{i=2}^{4} \frac{1}{2} M_{i,\max}^2 - \sum_{i=2}^{3} \lambda_{\min} (\mathbf{L}_i) \left\| \tilde{\mathbf{X}}_i \right\|^2 + \sum_{i=2}^{3} \frac{\hbar^2}{4} \left\| \tilde{\mathbf{X}}_i \right\|^2$$
$$+ \sum_{i=2}^{3} \frac{\hbar^2}{4} \left\| \tilde{\mathbf{W}}_{0,i}^{*} \right\|^2 + \sum_{i=2}^{3} \frac{1}{2} \left\| \tilde{\mathbf{X}}_i \right\|^2 + \sum_{i=2}^{3} \frac{1}{2} \varsigma_i^{*2}$$
$$+ \sum_{i=2}^{3} \left(\begin{array}{c} \frac{\hbar^2}{2} \lambda_{\max} (\Gamma_i) \left\| \tilde{\mathbf{X}}_i \right\|^2 + \frac{\lambda_{\max} (\boldsymbol{\varphi}_i)}{2} \Upsilon^2 + \\ \frac{\hbar^2 \lambda_{\max} (\Gamma_i) - \lambda_{\min} (\boldsymbol{\varphi}_i) + \lambda_{\max} (\boldsymbol{\varphi}_i)}{2} \left\| \tilde{\mathbf{W}}_{0,i}^{*} \right\|^2 \end{array} \right) \quad (74)$$

$$\le -\frac{\kappa_y \sigma_{b_y}^{2\bar{p}}}{1 - \sigma_{b_y}^{2\bar{p}}} - \frac{\kappa_z \sigma_{b_z}^{2\bar{p}}}{1 - \sigma_{b_z}^{2\bar{p}}} - \underbrace{\left(\lambda_{\min} (\boldsymbol{\kappa}_2) - \frac{\hbar^2}{4} - \frac{1}{2} \right)}_{\pi_{12}} \left\| \mathbf{e}_2 \right\|^2$$
$$- \underbrace{\lambda_{\min} (\boldsymbol{\kappa}_4)}_{\pi_{14}} \left\| \mathbf{E}_4 \right\|^2 - \underbrace{\left(\begin{array}{c} \lambda_{\min} (\boldsymbol{\kappa}_3) - \frac{\lambda_{\max} (\mathbf{B}_3)}{2} - \\ \frac{\hbar^2}{4} - \frac{1}{2} \end{array} \right)}_{\pi_{13}} \left\| \mathbf{e}_3 \right\|^2$$
$$- \underbrace{\left(\begin{array}{c} \frac{\lambda_{\min} (\boldsymbol{\Psi})}{\left\| \boldsymbol{\chi} \right\| + \delta} - \frac{\lambda_{\max} (\mathbf{B}_3)}{2} - \\ \lambda_{\max} (\mathbf{B}_4) \bar{U} \end{array} \right)}_{\pi_2} \left\| \boldsymbol{\chi} \right\|^2 - \sum_{i=2}^{4} \underbrace{\left(\frac{1}{\tau_i} - \frac{1}{2} \right)}_{\pi_{3i}, i=2,3,4} \left\| \boldsymbol{\varepsilon}_i \right\|^2$$
$$- \sum_{i=2}^{3} \underbrace{\frac{\lambda_{\min} (\boldsymbol{\varphi}_i) - \hbar^2 \lambda_{\max} (\Gamma_i) - \lambda_{\max} (\boldsymbol{\varphi}_i) - \hbar^2}{2}}_{\pi_{5i}, i=2,3} \left\| \tilde{\mathbf{W}}_{0,i}^{*} \right\|^2$$
$$- \sum_{i=2}^{3} \underbrace{\left(\begin{array}{c} \lambda_{\min} (\mathbf{L}_i) - \frac{\hbar^2}{4} - \\ \frac{1}{2} - \frac{\hbar^2}{2} \lambda_{\max} (\Gamma_i) \end{array} \right)}_{\pi_{4i}, i=2,3,4} \left\| \tilde{\mathbf{X}}_i \right\|^2 + \sum_{i=2}^{3} \underbrace{\left(\begin{array}{c} \frac{1}{2} M_{i,\max}^2 + \varsigma_i^{*2} + \\ \frac{\lambda_{\max} (\boldsymbol{\varphi}_i)}{2} \Upsilon^2 \end{array} \right)}_{\Xi}$$

$$= -\boldsymbol{\Lambda}^T \boldsymbol{\Pi} \boldsymbol{\Lambda} + \boldsymbol{\Xi}$$

where $\boldsymbol{\Xi}$ is bounded according to the analysis on the MLPESN and DSC filtering error above; and

$$\begin{cases} \mathbf{\Lambda}=\begin{bmatrix} \sigma_{b_y}^{2\bar{p}}\big/\!\left(1-\sigma_{b_y}^{2\bar{p}}\right), \sigma_{b_z}^{2\bar{p}}\big/1-\sigma_{b_z}^{2\bar{p}}, \mathbf{e}_2, \mathbf{e}_3, \mathbf{E}_4, \boldsymbol{\chi}, \\ \boldsymbol{\varepsilon}_2, \boldsymbol{\varepsilon}_3, \boldsymbol{\varepsilon}_4, \tilde{\mathbf{X}}_2, \tilde{\mathbf{X}}_3, \tilde{\mathbf{X}}_4, \tilde{\mathbf{W}}_{0,2}^*, \tilde{\mathbf{W}}_{0,3}^*, \tilde{\mathbf{W}}_{0,4}^* \end{bmatrix}^T \\ \mathbf{\Pi}=\mathrm{diag}\begin{pmatrix} \kappa_y, \kappa_z, \pi_{12}, \pi_{13}, \pi_{14}, \pi_2, \pi_{32}, \pi_{33}, \\ \pi_{34}, \pi_{41}, \pi_{42}, \pi_{43}, \pi_{52}, \pi_{53}, \pi_{54} \end{pmatrix} \end{cases} \quad (75)$$

Then we have

$$\dot{V} \le -\lambda_0 V + \mathbf{\Xi} \quad (76)$$

where $\lambda_0 = 2\lambda_{\min}(\mathbf{\Pi})$. Then, we conclude Eq. (76) with

$$0 \le V(t) \le V(0)\exp(-\lambda_0 t) + \frac{\Xi}{\lambda_0}\big(1-\exp(-\lambda_0 t)\big) \quad (77)$$

$$\le \frac{\Xi}{\lambda_0}, \forall t \ge t_0$$

Thus, with proper parameters selection, the diagonal matrix $\mathbf{\Pi}$ in Eq. (75) will be positive definite and $V(t)$ will be ultimately limited by Ξ/λ_0, if $\mathbf{\Pi}$ is tuned to be a positive definite. Then, all the errors are restricted in the compact set $\Omega=\{\mathbf{\Lambda}\,|\,V(t)\le\Xi/\lambda_0\}, \forall t \ge t_0$. The uniformly ultimately bounded stability of the closed-loop system can be ensured.

Furthermore, recalling the aBLF theory by K.P. Tee *et al.* [17] (Theorem 1) and Eqs. (37) - (38), it arrives that the time-varying terrain obstacle constraints (12) and (13) will never be violated by the towed vehicle's trajectory $\mathbf{X}_1$. ∎

IV. SIMULATION AND ANALYSIS

This section conducts numerical simulations to validate the performance of the proposed controller for the air-ground recovery system subject to terrain obstacles, unmeasurable cable tensions, trailing vortex, gusts, and actuator saturation. The towing aircraft is assumed to fly at the height of $H_0=280\,\mathrm{m}$ with $V_0=50\,\mathrm{m/s}$. The towed cable and vehicle parameters in [6,9] are adopted. The total length of the cable is set as $L_0=300\,\mathrm{m}$. Moreover, two recoveries scenarios are considered, where two ground targets are respectively located at the front and back of the two terrain obstacles, as shown in Fig. 1. To verify the robustness against the wind, the horizontal wind gust in a half sinusoidal form is considered, as shown by Eq. (78). The parameters for the terrain obstacles and the actuator saturation are listed in Table I.

$$w_{\mathrm{gust}}^y = \begin{cases} 10\sin\big((\pi x/V_0-0)/10\big), & 0 \le x \le 10V_0 \\ 0, & \text{otherwise} \end{cases} \quad (78)$$

To further verify the effectiveness of the proposed MLPESN-aBLF method, some comparisons with the existing methods on towed vehicle control have been conducted. Considering the relatively few works on towed vehicle control have been published, we choose the nonlinear feedback control law (NFCL) without disturbance observer [9] and the high order sliding mode observer (HOSMO) based DSC (HOSMO-DSC) method [6] for comparison below. This kind of selection can ensure the hierarchy of comparison to some

extent. The detailed formulation of the NFCL and HOSMO-DSC can be found in [9] and [6], respectively. Table II lists the parameters of the compared methods.

TABLE I
PARAMETERS OF THE ASSUMED TERRAIN OBSTACLES

Parameters	Values	Parameters	Values	Parameters	Values
H_{target}	2.0 m	h_0	8 m	$x_{target1}$	1000 m
$h_{t,1}$	30 m	$h_{t,2}$	20 m	$x_{target2}$	2000 m
$x_{to,1}$	$5V_0$ m	$x_{to,2}$	$25V_0$ m	$y_{target1}$	0 m
$x_{to,3}$	$35V_0$ m	$x_{to,4}$	$55V_0$ m	$y_{target2}$	0 m
$\bar{H}_{tolerant}$	1.0 m	$\underline{H}_{tolerant}$	1.0 m	$H_{target1}$	33.21 m
y_0	10 m	y_∞	0.1 m	$H_{target2}$	26.14 m
ℓ	0.4	$\bar{\delta}_a,\bar{\delta}_e,\bar{\delta}_r$	-25°	$\underline{\delta}_a,\underline{\delta}_e,\underline{\delta}_r$	-25°

TABLE II
PARAMETERS OF THE COMPARED METHODS

	Sections	Parameters and values
Proposed MLPESN-aBLF	DSC	$\tau_2=0.06,\ \tau_3=0.05,\ \tau_4=0.03$
	ESN	$\mathbf{L}_2=\mathrm{diag}(30,30),\ \mathbf{\Gamma}_2=\mathrm{diag}(2,2),$ $\boldsymbol{\varphi}_2=\mathrm{diag}(1,1),\ \mathbf{L}_3=\mathrm{diag}(50,50,50),$ $\mathbf{\Gamma}_3=\mathrm{diag}(2,2,2),\ \boldsymbol{\varphi}_3=\mathrm{diag}(0.5,0.5,0.5)$
	Controller	$\kappa_y=\kappa_y=1,$ $\bar{\kappa}_j(t)=\sqrt{\left(\dot{k}_{a_j}\big/k_{a_j}\right)^2+\left(\dot{k}_{b_j}\big/k_{b_j}\right)^2+\rho_j},$ $j=y,z\,,\ \rho_y=\rho_z=1,\ \bar{p}=3,$ $\mathbf{\kappa}_2=\mathrm{diag}(3,3),\ \mathbf{\kappa}_3=\mathrm{diag}(8,8,8),$ $\mathbf{\kappa}_4=\mathrm{diag}(20,20,20),$ $\mathbf{\Psi}=\mathrm{diag}(20,20,20),\delta=0.0001$
NFCL	Controller	$\mathbf{\kappa}_1=\mathrm{diag}(1,1),$ $\mathbf{\kappa}_2,\ \mathbf{\kappa}_3,\ \mathbf{\kappa}_4$ are same with MLPESN-aBLF
HOSMO-DSC	DSC	The DSC parameters are the same with MLPESN-aBLF
	HOSMO	$\mathbf{C}_2=\mathrm{diag}(100,100),\mathbf{C}_3=\mathrm{diag}(2,2,2)$
	Controller	$\mathbf{\kappa}_1=\mathrm{diag}(1,1),$ $\mathbf{\kappa}_2,\ \mathbf{\kappa}_3,\ \mathbf{\kappa}_4$ are same with MLPESN-aBLF

A. Scenario 1: Recovery for Target 1

Scenarios 1 considers the air-ground recovery for target 1 on the back of terrain obstacles, as shown in Fig. 1. With the dynamics of the towed cable-vehicle system in Sec.II, the equilibrium coordinate of the towed vehicle in the towing axis can be obtained: $\left(x_{D0}, y_{D0}, z_{D0}\right)=\left(-124.06, 0, -11.98\right)$. Two

This article has been accepted for publication in a future issue of this journal, but has not been fully edited. Content may change prior to final publication. Citation information: DOI 10.1109/TAES.2021.3101592, IEEE Transactions on Aerospace and Electronic Systems

> REPLACE THIS LINE WITH YOUR PAPER IDENTIFICATION NUMBER (DOUBLE-CLICK HERE TO EDIT) <   12

initial trajectory deviations are considered here: 1) Case 1: The initial trajectory of the towed vehicle is located at $\left(x_{D01}, y_{D01}, z_{D01}\right) = \left(-124.06, 7.756, -12.210\right)$; 2) Case 2: The initial trajectory of the towed vehicle is located at $\left(x_{D02}, y_{D02}, z_{D02}\right) = \left(-124.06, -3.874, -12.042\right)$.
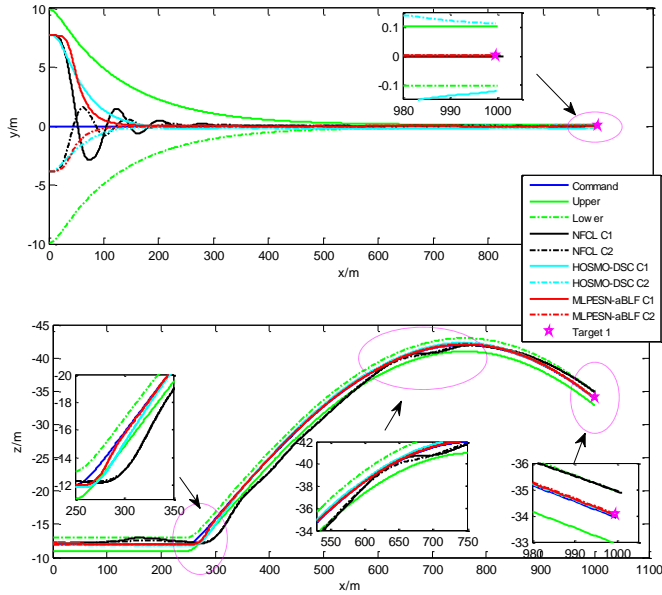
Fig. 3. Trajectory results with respect to x in Scenario 1.
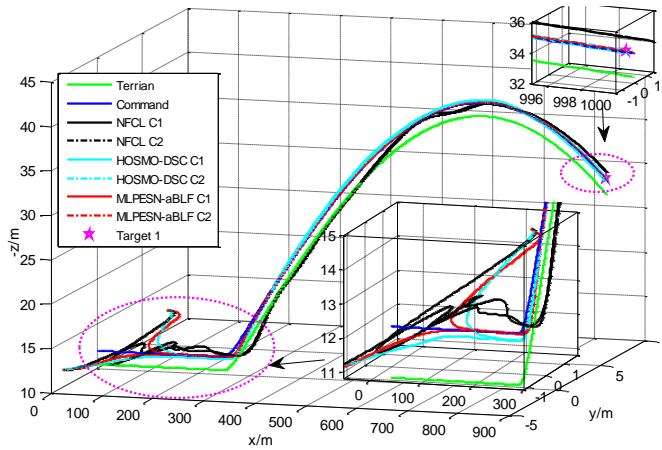
Fig. 4. The 3-D trajectory of the towed vehicle in Scenario 1.

Fig. 3 shows the towed vehicle's trajectory results in the inertial axis. With the proposed constrained flight controller, the lateral and vertical trajectories with respect to x exactly track the command signals. The trajectories are limited among the predefined constraint scopes, even under the towing, airflows, and initial trajectory derivations. Constraint violation never occurs throughout the recovery process. The reason for the constrained trajectories by the proposed method can be attributed to the aBLF mechanism. However, the constraint violations can be found in the results by NFCL and HOSMO-DSC methods which do not possess the constrained control mechanism. As shown in Fig. 3 and Fig. 4, the NFCL and HOSMO-DSC cannot always limit the trajectories within the predefined limitations, especially between the forward position $x=200$ to $x=300$. Moreover, the proposed method can ensure the towed vehicle exactly hook the ground target 1 at

the forward trajectory $x=1000$, which means the proposed controller can successfully recover the ground target 1 even when the terrain obstacles, unmeasurable cable tensions, trailing vortex wind gust, and actuator saturations exist. To better visualize the trajectory results and validate the air-ground recovery performance, Fig.4 shows the 3-D trajectory history of the towed vehicle, and Fig. 5 depicts the cable-vehicle's geometry at the time of recovery docking.
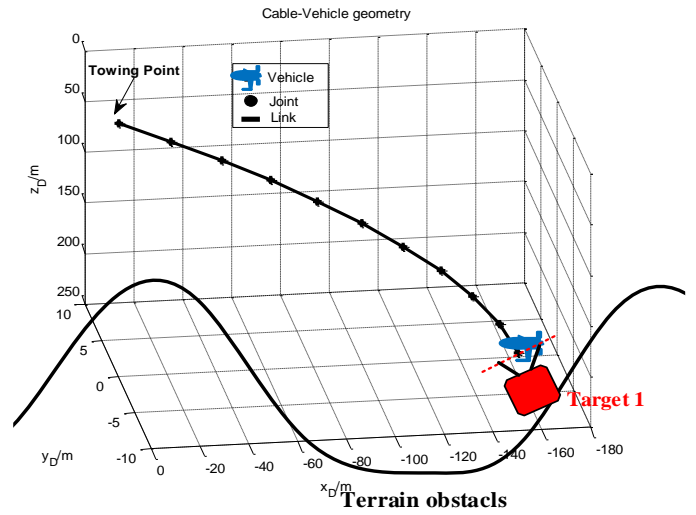

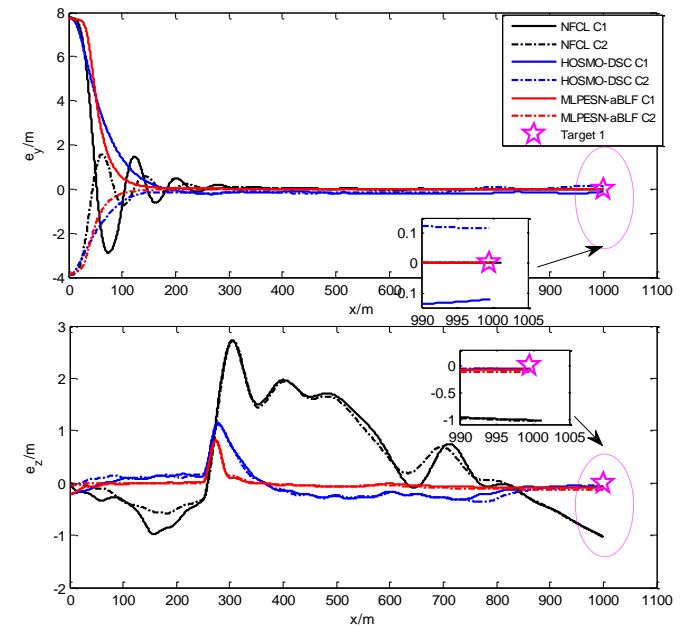Fig. 5. The cable-vehicle's geometry at the time of recovery docking with the proposed method (Scenario 1).

Fig. 6. The trajectory tracking errors with respect to x in Scenario 1.

The trajectory tracking errors with respect to x are shown in Fig.6. It is observed that the actual hooking error by the proposed method is very close to the target error (0, 0) m. While, the trajectory tracking error results by the compared methods, especially the NFCL method, are relatively larger. The proposed method can control the trajectory tracking error, especially the lateral derivation, which quickly converges to zero, in presence of the initial derivations. The maximum vertical tracking error occurs at the beginning of terrain 1, but quickly converges to zero. The final hooking accuracy is not

affected and remains at a high level. Fig. 7 shows the trajectory and velocity results with respect to time. The lateral trajectory V_y is approximately zero after the elimination of initial lateral derivation and V_z will varies within a small range due to the high-precision time-varying trajectory tracking in the vertical direction.
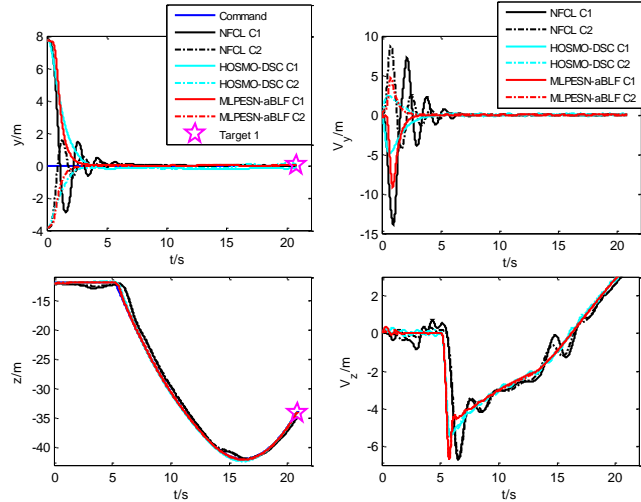

Fig. 7. The trajectory and velocity results with respect to time in Scenario 1.
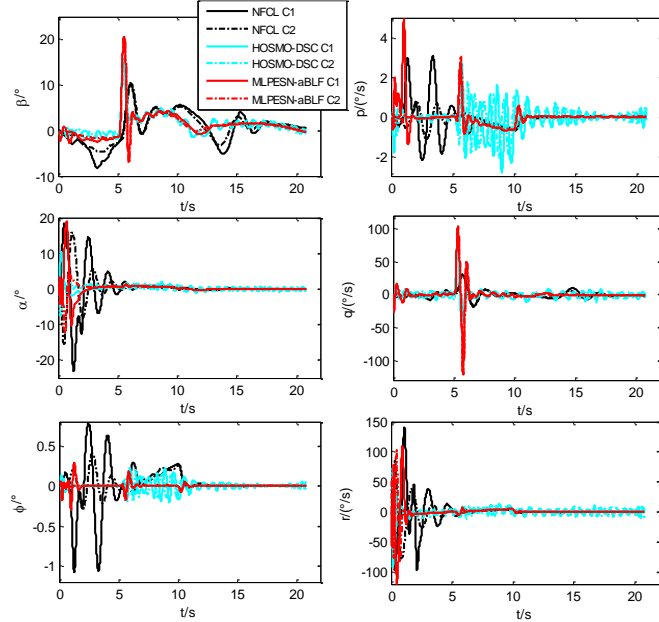

Fig. 8. The angular and angular rate results in Scenario 1.

Fig. 8 shows the results of sideslip angle, angle of attack, roll angle, and corresponding angular rate results. Fig. 9 illustrates the aerodynamic control inputs, which show that the actuator saturation occurs at the initial derivation elimination stage (t=0 s) and the beginning of terrain 1(t=5.0 s). With the compensation by the additional system in Eq. (47), the inputs δ_e, δ_r come out of the saturation phase in a very short time (t=0.8 s, t=5.5 s). It's demonstrated that the closed-loop system remains stable even under actuator saturation, and the proposed controller effectively recovers its tracking performance once it leaves the saturation stage.
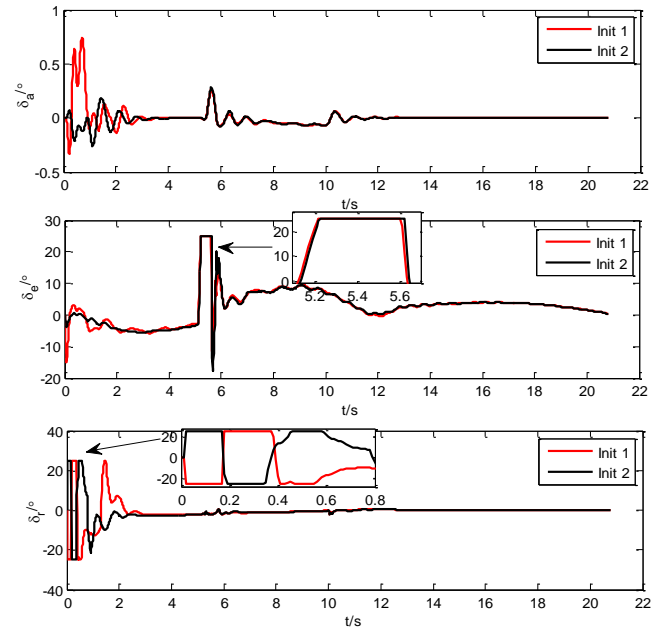

Fig. 9. The actuator control input results with the proposed method (Scenario 1).

B. Scenario 2: Recovery for Target 2

Scenarios 2 considers the air-ground recovery for target 2 located at the front of terrain obstacles, as shown in Fig. 2. The two initial trajectory deviations in Scenarios 1 are also considered here.
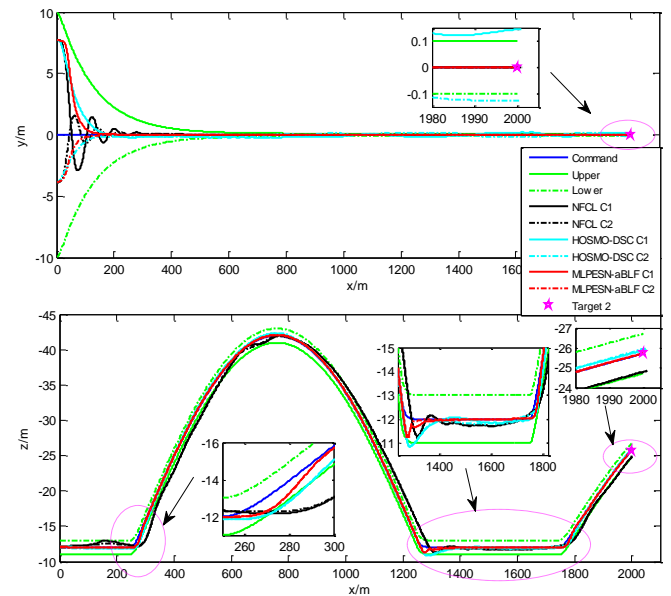

Fig. 10. Trajectory results with respect to x in Scenario 2.

Fig. 10 shows the towed vehicle's trajectory results in the inertial axis, Fig.11 shows the 3-D trajectory of the towed vehicle, and Fig. 12 shows the cable-vehicle's geometry at the time of recovery docking. From Fig.10 to 12, it can conclude that the proposed method achieves safe and accurate recovery of target 2 on the back of terrain obstacles, even with the terrain obstacles, unmeasurable cable tensions, trailing vortex wind gust, actuator saturations, and initial trajectory derivations. However, the constraint violations may occur in the results by NFCL and HOSMO-DSC methods. The vehicle's trajectory

can accurately track the time-varying command signal and never violate the time-varying terrain constraints throughout the recovery. The vehicle exactly hooks the ground target 2 at the forward position $x=2000$.
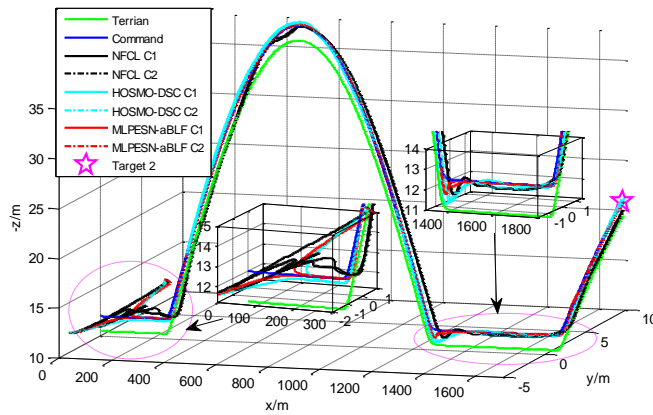

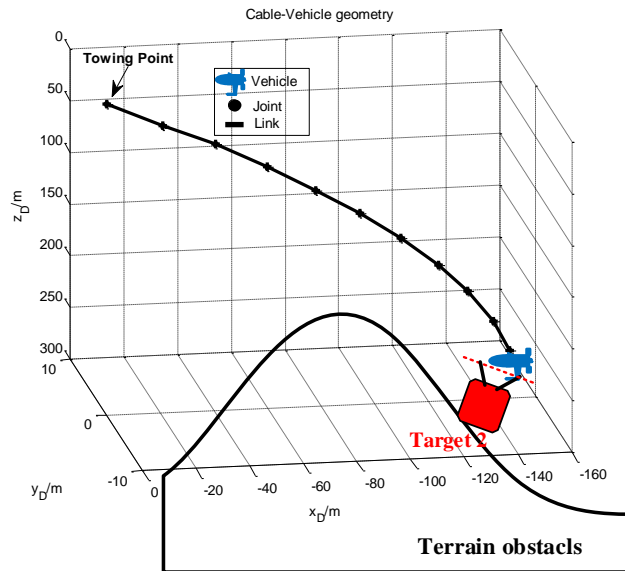Fig. 11. The 3-D trajectory of the towed vehicle in Scenario 2.

Fig. 12. The cable-vehicle geometry at the time of recovery docking with the proposed method (Scenario 2).

Fig.13 shows the trajectory tracking errors, from which it also can be seen that the proposed method can offer a smaller hooking error at the hooking position $x=2000$. While, the trajectory tracking error results by the compared methods are relatively larger. The trajectory, velocity, angular and angular rates are shown in Fig. 14 to Fig. 15. Fig.16 gives the vehicle's aerodynamic control inputs. As Fig. 16 shown, although the actuator saturation occurs at the initial derivation elimination stage ($t=0$ s) and the beginning of terrain 1($t=5.0$ s) and terrain 2($t=35.0$ s), the proposed controller can immediately guide the inputs to jump out the saturation to ensure the system's stability and the control performance recovery.

Based on simulation comparison results and analysis above, it can be observed that the effectiveness of the proposed MLPESN-aBLF constrained flight controller in terms of the constrained control performance, terrain avoidance ability, and robustness.
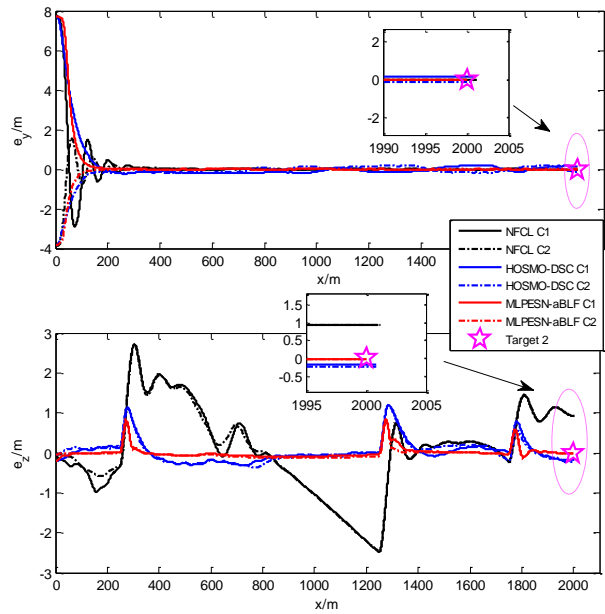

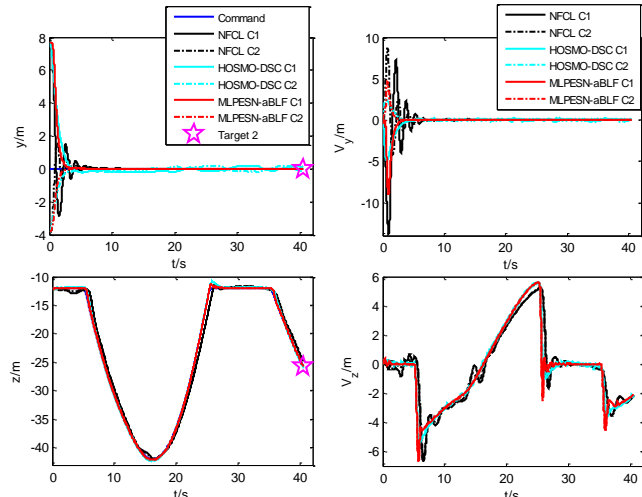Fig. 13. The trajectory tracking errors with respect to x in Scenario 2.

Fig. 14. The trajectory and velocity results with respect to time in Scenario 2.
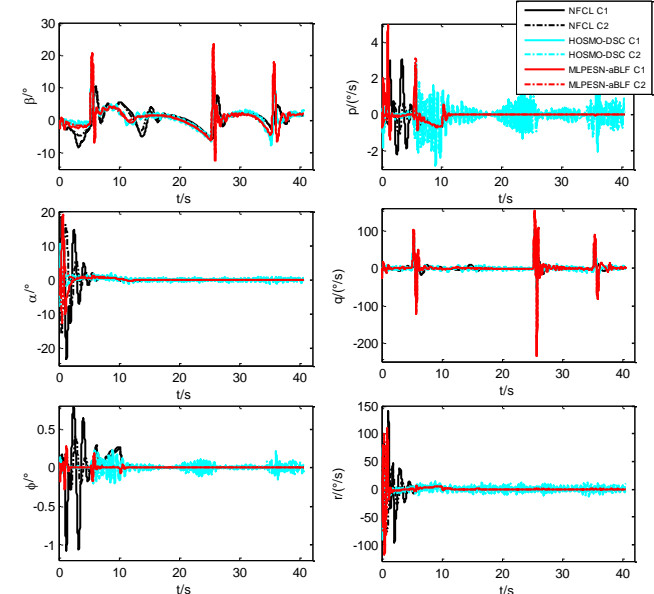

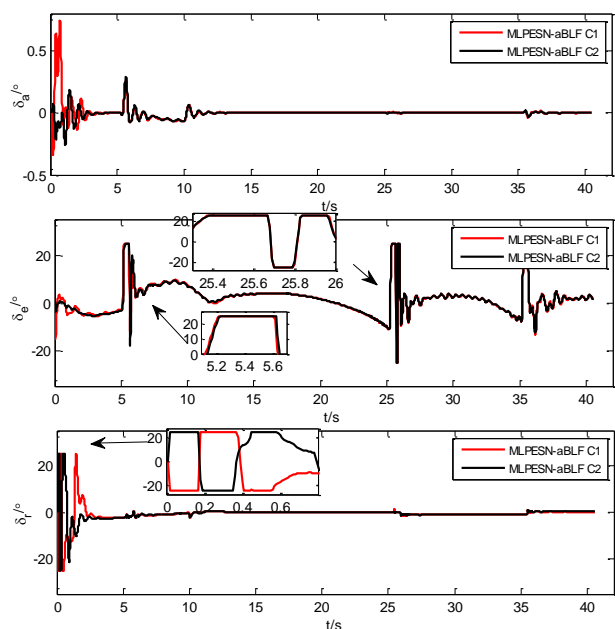Fig. 15. The angular and angular rate results in Scenario 2.

This article has been accepted for publication in a future issue of this journal, but has not been fully edited. Content may change prior to final publication. Citation information: DOI 10.1109/TAES.2021.3101592, IEEE Transactions on Aerospace and Electronic Systems

> REPLACE THIS LINE WITH YOUR PAPER IDENTIFICATION NUMBER (DOUBLE-CLICK HERE TO EDIT) <   15

Fig. 16. The actuator control input results with the proposed method (Scenario 2).

V. CONCLUSION

In this research, the MLPESN-based neural-adaptive constrained flight controller is proposed for the air-ground recovery system when the terrain obstacles, unmeasurable cable tensions, trailing vortex, wind gust, and actuator saturations exist. The cable-vehicle system's dynamics and the air-ground recovery problem under terrain obstacles are formulated. The aBLF based constrained trajectory control strategy is innovatively presented to avoid the terrain obstacles, by transforming the terrain violations into time-varying constraints on the vehicle's trajectory. The control input saturation is addressed with an established auxiliary system. The MLP-ESN approximators are constructed to accurately approximate the lumped unknown dynamics caused by the cable towing and airflows. The effectiveness of the proposed algorithm is verified under two recovery scenarios. The proposed algorithm is also applicable to generalized aerial towed vehicles or drogues.

REFERENCES

[1] L. Sun, J. Castagno, J. Hedengren and R. Beard, "Parameter estimation for towed cable systems using moving horizon estimation," *IEEE Trans. Aerosp. Electron. Syst.*, vol. 51, no. 2, pp. 1432-1446, Apr. 2015.

[2] P. Williams, D. Sgarioto and P. Trivailo, "Optimal control of an aircraft-towed flexible cable system," *J. Guid. Control. Dynam.*, vol. 29, no. 2, pp. 401–410, May.-Jun. 2007.

[3] Y.W. Jun, K.R. Hall, A.G. Bennett and P.D. Bridges, "Optimal guidance for airborne cable pickup system," *in Proc. 17th Fluid Dynam., Plasma Dynam., and Lasers Conf.,* AIAA Paper 84-1893, Aug. 1984.

[4] X. Dai, Z. Wei, Q. Quan, and K. Cai, "Hose-drum-unit modeling and control for probe-and-drogue autonomous aerial refueling," *IEEE Trans. Aerosp. Electron. Syst.,* vol. 56, no. 4, pp. 2779-2791, Aug. 2020.

[5] H. Duan, Y. Sun and Y. Shi, "Bionic visual control for probe-and-drogue autonomous aerial refueling," *IEEE Trans. Aerosp. Electron. Syst.,* Oct. 2020, DOI: 10.1109/TAES.2020.3034026.

[6] Z. Su, C. Li, Y. Liu, "Anti-disturbance dynamic surface trajectory stabilization for the towed aerial recovery drogue under unknown airflow disturbances," Mech. Syst. Signal Process., vol. 150, 107342, Mar. 2021.

[7] V. Varadarajan and J. Krolik, "Array shape estimation and tracking using active sonar reverberation," *IEEE Trans. Aerosp. Electron. Syst.,* vol. 40, no. 3, pp. 1073–1086, Jul. 2004.

[8] J.E. Cochran, M. Innocenti, T.S. No and A. Thukral, "Dynamics and control of maneuverable towed flight vehicles," *J. Guid. Control. Dynam.,* vol. 15, no. 5, pp. 1245-1252, Sep.-Oct. 1992.

[9] A.S. Bourmistrov, R.D. Hill and P. Riseborough, "Nonlinear control law for aerial towed target," *J. Guid. Control. Dynam.,* vol. 18, no. 6, pp. 1232-1238, Nov.-Dec. 1995.

[10] P. Williams, "Optimal terrain-following for towed-aerial-cable sensors," *Multibody Syst. Dyn.,* vol. 30, pp. 351-374, Oct. 2006.

[11] P. Williams and P. Trivailo, "Dynamics of circularly towed cable systems, Part 2: Transitional flight and deployment control," *J. Guid. Control. Dynam.,* vol. 30, no. 3, pp. 766-779, Mar.-Apr. 2006.

[12] Central Intelligence Agency, "Robert Fulton's skyhook and operation coldfeet," https://www.cia.gov/library/center-for-the-studyof-intelligence/csi-publications/csi-studies/studies/95unclass/Leary.html (Sept. 2010)

[13] J.W. Nichols, L. Sun, R.W. Beard and T. Mclain, "Aerial rendezvous of small unmanned aircraft using a passive towed cable system," *J. Guid. Control. Dynam.*, vol. 37, no. 4, pp. 1131-1142, Jul.-Aug. 2014.

[14] Z. Liu, J. Liu and W. He, "Modeling and vibration control of a flexible aerial refueling hose with variable lengths and input constraint," *Automatica*, vol. 77, pp. 302-310, Mar. 2017.

[15] W. He, Y. Chen and Y. Zhao, "Modeling and vibration control of a flexible aerial refueling hose with variable lengths and input constraint," *IEEE Trans. Cybenetics.*, vol. 46, no. 3, pp. 620-629, Mar. 2016.

[16] Z. Su, C. Li and Z. Zhen, "Anti-disturbance constrained control of the air recovery carrier via an integral barrier Lyapunov function," *Aerosp. Sci. Technol.,* vol. 106, pp. 106157, Nov. 2020.

[17] K.P. Tee, B.B. Ren and S.S. Ge, "Control of nonlinear systems with time-varying output constraints," *Automatica*, vol. 47, pp. 2511-2516, Sep. 2011.

[18] D. Swaroop, J.K. Hedrick, P.P. Yip and J.C. Gerdes, "Dynamic surface control for a class of nonlinear systems," *IEEE Trans. Automat. Contr.*, vol. 45, no. 10, pp. 1893-1899, Oct. 2000.

[19] M. Chen, G. Tao and B. Jiang, "Dynamic surface control using neural networks for a class of uncertain nonlinear systems with input saturation," *IEEE Trans. Neural Netw.,* vol. 26, no. 9, pp. 2086-2097, Sep. 2015.

[20] X. Shao, N. Liu, J. Liu, H. Wang, "Model-assisted extended state observer and dynamic surface control based trajectory tracking for quadrotors via output feedback mechanism," *Int. J. Robust Nonlinear Control.,* vol. 28, pp. 2404-2423, 2018.

[21] W. Chen, "Disturbance observer-based control for nonlinear systems," *IEEE/ASME Trans. Mech.,* vol. 9, pp. 706-710, 2004.

[22] L. Guo, W. Chen, "Disturbance attenuation and rejection for systems with nonlinearity via DOBC approach," *Int. J. Robust Nonlinear Control.,* vol. 15, pp. 109-125, 2005.

[23] L. Guo, S. Cao, "Anti-disturbance control theory for systems with multiple disturbances: A survey," *ISA Transactions,* vol. 53, pp. 846-849, 2014.

[24] Z. Zhen, C. Yu, S. Jiang and J. Jiang, "Adaptive super-twisting control for automatic carrier landing of aircraft," *IEEE Trans. Aerosp. Electron. Syst.,* vol. 56, no. 2, pp. 984-997, Apr. 2020.

[25] J. Shin, "Adaptive dynamic surface control for a hypersonic aircraft using neural networks," *IEEE Trans. Aerosp. Electron. Syst.,* vol. 53, no. 5, pp. 2277-2289, Oct. 2017.

[26] X, Shao, Y. Shi and W. Zhang, "Adaptive dynamic surface control for a hypersonic aircraft using neural networks," *IEEE Trans. Aerosp. Electron. Syst.,* DOI 10.1109/TAES.2020.3040519, 2020.

[27] W. Chen, "Nonlinear disturbance observer enhanced dynamic inversion control of missiles," *J. Guid. Control. Dynam.*, vol. 18, no. 6, pp. 1232-1238, Nov.-Dec. 1995.

[28] J. Yang, S. Li, C. Sun, L. Guo, "Nonlinear-Disturbance-Observer-Based Robust Flight Control for Airbreathing Hypersonic Vehicles," *IEEE Trans. Aerosp. Electron. Syst.*, vol. 49, no. 2, pp. 1263-1275, Dec. 2013.

[29] C. Wang, L. Guo, C. Wen, X. Yu, J. Huang, "Attitude coordination control for spacecraft with disturbances and event-triggered communication," *IEEE Trans. Aerosp. Electron. Syst.*, vol. 57, no. 1, pp. 586-596, Dec. 2021.

[30] S. Zhou, K. Guo, X. Yu, L. Guo, L. Xie, " Fixed-time Observer Based Safety Control for a Quadrotor UAV," *IEEE Trans. Aerosp. Electron. Syst.*, DOI 10.1109/TAES.2021.3068434, 2021.

This article has been accepted for publication in a future issue of this journal, but has not been fully edited. Content may change prior to final publication. Citation information: DOI 10.1109/TAES.2021.3101592, IEEE Transactions on Aerospace and Electronic Systems

> REPLACE THIS LINE WITH YOUR PAPER IDENTIFICATION NUMBER (DOUBLE-CLICK HERE TO EDIT) <   16

[31] X. Wen, L. Guo, P. Yan, "Composite hierarchical anti-disturbance control for robotic systems with multiple disturbances," *Int. J. Control. Autom.*, vol. 12, no. 3, pp. 541-551, 2014.

[32] N. Wang, H. Wu, L. Guo, "Coupling-observer-based nonlinear control for flexible air-breathing hypersonic vehicles," *Nonlinear Dyn.*, vol. 78, pp. 2141-2159, 2014.

[33] A. Aboudonia, R. Rashad, A. EI-Badawy, "Composite hierarchical anti-disturbance control of a quadrotor UAV in the presence of matched and mismatched disturbances," *J. Intell. Robot. Sys*, vol. 90, pp. 201-216, 2018.

[34] H. Lu, C. Liu, L. Guo, W. Chen, "Constrained anti-disturbance control for a quadrotor based on differential flatness," *Int. J. Syst. Sci.*, vol. 48, no. 6, pp. 1182-1193, 2017.

[35] H. Sun and L. Guo, "Neural network-based DOBC for a class of nonlinear systems with unmatched disturbances, " *I IEEE Trans. Neural Netw.*, vol. 28, no. 2, pp. 482-489, Feb. 2017.

[36] Y. Pan and J. Wang, "Model predictive control of unknown nonlinear dynamical systems based on recurrent neural networks, " *IEEE Trans. Ind. Electron.*, vol. 59, no. 8, pp. 3089-3101, Aug. 2012.

[37] G. Sun, D. Li and X. Ren, "Modified neural dynamic surface approach to output feedback of MIMO nonlinear systems," *IEEE Trans. Neur. Net. Lear.*, vol. 26, no. 2, pp. 224-236, Feb. 2015.

[38] S. Wang, J. Na and X. Ren, "RISE-based asymptotic prescribed performance tracking control of nonlinear servo mechanisms," *IEEE Trans. Syst., Man, Cybern., Syst.*, vol. 48, no. 12, pp. 2359-2370, Feb. 2018.

[39] A. Deihimi, A. Rahmani, "Application of echo state network for harmonic detection in distribution networks," *IET Renew. Power Gener.,* vol. 11, no. 5, pp. 1094-1101, Jan. 2017.

[40] Y. Pan and J. Wang, "Model predictive control of unknown nonlineardynamical systems based on recurrent neural networks, " *IEEE Trans. Ind. Electron.,* vol. 59, no. 8, pp. 3089-3101, Aug. 2012.

[41] X, Shao, Y. Shi, W. Zhang and H. Cao, " Neurodynamic approximation-based quantized control with improved transient performances for MEMS gyroscopes: theory and experimental results," *IEEE Trans. Ind. Electron.,* DOI 10.1109/TIE.2020.3026297, 2020.

[42] M. Chen, S.S. Ge and B.B. Ren, "Adaptive Tracking Control of Uncertain MIMO Nonlinear Systems with Input Constraints," *Automatica*, vol. 47, pp. 452-465, Mar. 2011.

[43] Q. Zong, F. Wang, B. Tian and R. Su, "Robust adaptive dynamic surface control design for a flexible air-breathing hypersonic vehicle with input constraints and uncertainty," *Nonlinear Dynam.,* vol.78, pp. 289-315, May. 2014.

[44] R. Wang, and J. Liu, "Trajectory tracking control of a 6-DOF quadrotor UAV with input saturation via backstepping," *J. Frankl. Inst.*, vol. 355, pp. 3288-3309, Mar. 2018.

[45] B. Xu, X. Wu, D. Wei, and J. Huang, "Neural-approximation-based robust adaptive control of flexible air-breathing hypersonic vehicles with parametric uncertainties and control input constraints," *Information Sciences*, vol. 346-347, pp. 29-73, 2016.

[46] B. Xu, X. Huang, D. Wang, and F. Sun, "Dynamic surface control of constrained hypersonic flight models with parameter estimation and actuator compensation," *Asian J. Control*, vol. 16, no. 1, pp. 162–174, 2014.

[47] X. Bu, D. Wei and G. He, "A robust constrained control approach for flexible air-breathing hypersonic vehicles," *Int. J. Robust Nonlin.*, vol. 30, no, 7, pp. 2752-2776, May. 2020.

[48] B. Etkin, *Dynamic of Atmospheric Flight, 1st ed*. New York, NY, USA: John Wiley & Sons, pp. 93–396, 1972.

Biography
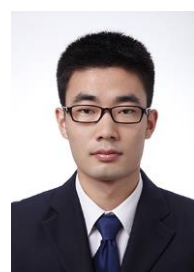
Zikang Su was born in Anhui, China, in 1990. He received the B.E. degree from China University of Mining and Technology, Xuzhou, China, and the Ph.D. degree from Beihang University (BUAA), Beijing, China, in 2012 and 2018, respectively. In 2018, he joined the College of Automation Engineering, Nanjing University of Aeronautics and Astronautics (NUAA). He is currently an assistant professor with NUAA. His research interests include autonomous flight control and intelligent decision of unmanned aerial vehicles.

Xinwei Wang received his B.S. and Ph.D. degrees in Aerospace Engineering from Beihang University, Beijing, China in 2013 and 2019, respectively. He was a research assistant at Queen Mary University of London, the U.K. from 2019 to 2020. He is now a postdoc researcher at TU Delft, the Netherlands. His current interests include space systems and intelligent transport systems.

Honglun Wang was born in Shaanxi, China, in 1970. He received the B.E., M.E., and Ph.D. in Fire Control from Northwestern Polytechnical University, China, in 1992, 1995 and 1998. From 1998 to 2000, he did postdoctoral research at Nanjing University of Aeronautics and Astronautics, China. He is currently a professor affiliated with Navigation, Guidance and Control at Beihang University (BUAA). He was chosen by the New Century Excellent Researcher Award Program from Ministry of Education of China in 2009. His research interests include autonomous flight control for UAVs, sense and avoid technology for UAVs, and theory and method of path planning in complex environments for UAVs